

Title: Self-supervised learning for label-free segmentation in cardiac ultrasound

Authors: Danielle L. Ferreira PhD¹, Zaynaf Salaymang RDCS², Rima Arnaout MD^{3*}

¹Department of Medicine, Division of Cardiology
Bakar Computational Health Sciences Institute
University of California, San Francisco
521 Parnassus Avenue
San Francisco, CA 94143

²Department of Medicine, Division of Cardiology
505 Parnassus Avenue
San Francisco, CA 94143

³Department of Medicine, Division of Cardiology
Bakar Computational Health Sciences Institute
UCSF-UC Berkeley Joint Program in Computational Precision Health
Department of Radiology, Center for Intelligent Imaging
University of California, San Francisco
521 Parnassus Ave Box 0124
San Francisco, CA 94143

* Corresponding Author

Short title: Self-supervised learning for cardiac ultrasound

KEYWORDS: deep learning, machine learning, semantic segmentation, self-supervised learning, cardiovascular imaging, ultrasound.

WORD COUNT: 3708

Abstract

Segmentation and measurement of cardiac chambers is critical in cardiac ultrasound but is laborious and poorly reproducible. Neural networks can assist, but supervised approaches require the same laborious manual annotations. We built a pipeline for self-supervised (no manual labels) segmentation combining computer vision, clinical domain knowledge, and deep learning. We trained on 450 echocardiograms (93,000 images) and tested on 8,393 echocardiograms (4,476,266 images; mean 61 years, 51% female), using the resulting segmentations to calculate biometrics. We also tested against external images from an additional 10,030 patients with available manual tracings of the left ventricle. r^2 between clinically measured and pipeline-predicted measurements were similar to reported inter-clinician variation and comparable to supervised learning across several different measurements (r^2 0.56-0.84). Average accuracy for detecting abnormal chamber size and function was 0.85 (range 0.71-0.97) compared to clinical measurements. A subset of test echocardiograms ($n=553$) had corresponding cardiac MRIs, where MRI is the gold standard. Correlation between pipeline and MRI measurements was similar to that between clinical echocardiogram and MRI. Finally, the pipeline accurately segments the left ventricle with an average Dice score of 0.89 (95% CI [0.89]) in the external, manually labeled dataset. Our results demonstrate a manual-label free, clinically valid, and highly scalable method for segmentation from ultrasound, a noisy but globally important imaging modality.

Introduction

Artificial intelligence (AI) has the potential to revolutionize medical imaging. The revolution will not be supervised¹.

Nowhere is the potential for AI, as well as the burden of supervised learning, more clear than for cardiac ultrasound, the primary cardiac imaging modality². The quantification of chamber size, mass, and function are critical to diagnosis, prognosis, and management³. However, this quantification is laborious, requiring several manual annotations per exam. Furthermore, even when performed by experts, manual annotations can be susceptible to inter- and intra-observer variability given the low spatial resolution and artifacts inherent to ultrasound imaging⁴.

Measurement variability can compound e.g. when linear and area measurements are used to calculate volumes and function^{5,6}. Finally, despite the importance of structural and functional measurements for all chambers³, the right heart and left atrium are often neglected in practice, in large part due to the laborious nature of performing additional annotations.

To overcome these challenges, researchers have turned to deep learning-based semantic segmentation. To date, supervised approaches have been used for this task⁷⁻⁹, but these require the same manual annotations mentioned above. Therefore, supervised segmentation does not alleviate labeling burden, and instead raises additional concern of using variable and error-prone manual annotations as ground-truth¹⁰. In fact, to mitigate potential bias from any one person, multiple labelers are advocated, which further increases the cost of labeling¹¹; an entire industry has arisen to perform manual labeling¹². Manual labeling also scales poorly with each additional structure to be labeled, perhaps explaining why most studies of semantic segmentation of the heart to date have focused on the left ventricle^{9,13-15}. Emerging foundation models for segmentation of photographic images do not obviate manual labeling (some requiring over a billion manual annotations)¹⁶, require additional manual input at the point of use, and do not work well on ultrasound without additional labor¹⁷.

Self-supervised learning (SSL) has the potential to obviate these problems. SSL networks are trained with automatically generated labels and human annotation is not required^{1,18-2021}. SSL has been used to segment objects in photographic imaging with some success²², but has been rare in biomedical imaging to date due to the low acceptable margin of error required for such applications^{23,24} (Fig. S1). In noisy ultrasound, automated segmentation has proved to be especially challenging²⁵⁻²⁷.

To bridge the gap between supervised segmentation and the challenges of ultrasound imaging, we hypothesized that weak labels could be created using computer vision techniques, circumventing both the time-consuming and subjective nature of human labels. We further hypothesized that using these labels in a self-supervised deep learning pipeline designed to mitigate overfitting and incorporate clinical domain knowledge could segment echocardiograms with performance rivaling clinicians.

Methods

Overview. Echocardiogram images were used to develop a self-supervised pipeline (Fig. 1) for cardiac chamber segmentation of the apical-2chamber (A2C), apical 4-chamber (A4C), and short-axis mid (SAX) views. Initial weak labels derived from computer vision techniques together with aggregate statistical information about chamber shapes and relationships were created (Supplemental Methods). These were used to train the neural networks described below and in Figure 1 in a series of early-learning and self-learning steps to arrive at a final prediction. The pipeline's final segmentation predictions were used to calculate structural and functional measurements according to clinical guidelines.

Datasets. *Internal dataset.* A total of 8,843 unique deidentified echocardiograms from UCSF were used (Table 1), with waived consent in compliance with the UCSF IRB. All clinically interpretable studies were included regardless of image quality. A2C, A4C and SAX b-mode views were identified as previously described²⁸. Views with color Doppler or LV contrast were excluded. For training and validation datasets, only images with a 200mm field of view (FoV) were included. Only images from the first heart cycle were used to reduce image-level redundancy²⁹. *Training and validation.* 2,228 videos (A2C, A4C, and SAX; 93,000 images) from 450 echocardiograms were used. Eighty percent were used for training and 20% for validation. *Testing.* 8,393 echocardiograms (4,476,266 images) were used as a holdout test set.

Measurements, such as left ventricle (LV) ejection fraction (LVEF), LV end-diastolic volume (LVEDV), LV end-systolic volume (LVESV), LV mass index (LVMI), left atrial (LA) volume, right atrial (RA) volume, and right ventricular end-diastolic area (RVEDA) were extracted from the echocardiogram database and used as ground-truth for performance evaluation for test echocardiograms. Where indicated, measurements were indexed by body surface area.

Additionally, for echocardiograms with corresponding CMRs, corresponding measurements were extracted from the clinical CMR reports. To evaluate test performance for a given chamber, only studies with available clinical measurements were used (Figure S1). Training, validation, and test sets did not overlap by image, patient, or study.

External dataset. An external test dataset was obtained from (<https://echonet.github.io/dynamic/>). It consisted of 20,060 A4C images from 10,030 patients (one systolic and one diastolic image per patient), with manually annotated clinical tracings of

the left ventricle, as well as a computer-estimated LVEF, LVESV, and LVEDV for each patient. Pixel size, alternative views, and manual tracings of LA, RA, and RV were not available.

Data preprocessing and initial weak label extraction. The ultrasound region of interest was extracted from DICOM images and normalized to a size of 0.5mm/pixel and resized to 256x256 pixels for segmentation networks or to 480x480 pixels for edge detection networks. Pixel intensities were normalized from 0 to 1. Computer vision and clinical knowledge techniques for initial weak label extraction are detailed in the Supplement. Preprocessing used Python 3.6 libraries OpenCV v4.4(<https://opencv.org/>), scikit-image (<https://scikit-image.org/>), Scipy (<https://pypi.org/project/scipy/>) and NumPy v1.20 (<https://numpy.org>).

Neural network architectures. Segmentation. A UNet was used for segmentation as described³⁰ with the following modifications: the 1x1 output layer was sigmoid-activated, Adam optimizer was set with a learning rate of 1e-4, soft dice loss and batch size 32 were used. Data augmentation consisted of random modifications to ~20 percent of training data as follows: rotations from 0-10 degrees, width and height shifts $\pm 10\%$ zoom $\pm 20\%$, shear 0-0.03, horizontal flips, contrast stretching between 2nd and 98th percentile, cropping of 160x160 pixel patches, downscale from 0.25 to 0.5, pixel dropout of 0.1, median blur, Gaussian noise with zero mean and variance between 0.03 and 0.2, contrast limited adaptive histogram equalization with upper threshold value for contrast limiting of 0.02, and random tone curve with scale of 0.1.

Edge-detection network. A holistically nested edge detection (HED) network was implemented for edge-detection tasks as described³¹ with the following modifications: the model was initialized with ImageNet weights and fine-tuned using the same hyperparameters as in Xie et al³² with a batch size 8. The following data augmentations were randomly applied: rotations 0-10 degrees, width and height shifts $\pm 10\%$, zoom $\pm 8\%$, shear 0-0.03, and horizontal flips.

Models were implemented in Keras 2.2.4 (<https://keras.io/>, [GitHub, 2015](#)) with TensorFlow 1.15.2 (<https://www.tensorflow.org/>) backend and trained in a NVIDIA Tesla M60 GPU with 8GiB of memory.

Early learning correction during network training. Deep neural networks have been observed to be robust to label noise and first fit the training data with clean labels during the early learning phase, before eventually memorizing the examples with false labels or artifacts³³⁻³⁷. We therefore exploited early learning in training the segmentation networks used in this study.

During network training, the transition between the early learning and memorization phases was

detected by monitoring the soft dice loss curve for the validation dataset. Training was stopped at this transition.

Self-learning during network training. In several neural network training steps, a neural network trained on a portion of training data with available weak labels was then used to infer on *all* available training and validation data in a self-learning manner³⁸, to recruit additional labeled training examples.

Quality control for segmentations during network training. At each step in the pipeline (Fig. 1), resultant segmentation labels were evaluated by shape descriptor analysis, discarding chambers of unreasonable size, eccentricity, or geometric chamber relationships as in Supplemental Methods.

Clinical calculations. The outputs of the segmentation pipeline were used to compute chamber dimensions, i.e., areas and volumes, for A2C, A4C and SAX views according to clinical guidelines³ with the following exception: in the external dataset, LVEF was estimated from the A4C view only, as a ratio of pixel areas/pixel lengths.

For each metric, we inferred the segmentation model in all frames of all videos that included the chamber of interest. Systolic and diastolic frames were automatically detected by plotting areas of each chamber segmentation by frame for all videos³⁹ and a sinusoid with heart rate frequency was fitted to these data. Then, the r^2 between the area by frame and its sinusoid fitting was used to select the video with the best periodic function per patient. The frame with the largest area of the chosen video by the r^2 method was selected to be the diastole, and the smallest frame of the same video to be the systole. (This was done to avoid videos in which the heart may drift in and out of view, which is not uncommon in clinical practice.) This method failed on less than 2% of the entire dataset, in which cases diastole and systole frames were manually chosen.

Statistical Analysis. Pearson correlation was used to measure the linear relationship between chamber measurements. Linear regression analyses were performed to measure the strength of these relationships. Bland-Altman (BA) plots were analyzed to demonstrate the bias and 95% limits of agreement (two standard deviations) between different methods for each measurement. Cohen's Kappa was used to assess the agreement between the normal and abnormal values determined by different measurement methods (e.g., clinical vs SSL).

Mann Whitney U testing was performed for patient demographics but not reported because due to dataset size, even minimal differences were found to be statistically significant. For r , r^2 , and Dice, 95% confidence intervals were computed by bootstrapping 10,000 iterations, however, CI were so narrow that they are not reported. All statistical testing was performed using the scipy package (<https://pypi.org/project/scipy/>) in Python 3.

Code Availability. Code will be made available upon publication at github.com/ArnaoutLabUCSF/CardioML

Data Availability. Training data are not publicly available because they contain protected patient health information. Test data is available at <https://echonet.github.io/dynamic/>

Results

Overview. We developed a pipeline (Fig. 1) to provide self-supervised segmentation of echocardiograms. We first extracted weak labels for cardiac chambers using traditional computer vision techniques and clinical shape priors (Methods, Supplemental Methods). We then used these weak labels to train more accurate segmentations, utilizing early stopping and clinical domain-guided label refinement in successive training steps to achieve final performance. Segmentation predictions from the final step were used to calculate biometrics for each chamber³, focusing on the most clinically relevant⁴⁰ views: the apical 2-chamber (A2C), apical 4-chamber (A4C), and short-axis mid (SAX).

We used 93,000 images from 450 transthoracic echocardiograms for training and validation and 4,476,266 images from 8,393 echocardiograms for testing, across a range of image qualities, pathologies, and patient characteristics (Table 1, “all-comers”). A subset of all-comers (n=553) had corresponding cardiac MRI (CMR) available within 30 days for additional comparison among to CMR, as CMR is considered the gold standard for cardiac measurements (Table 1, “CMR subset”). We also tested our pipeline against an external dataset of A4C images with an additional 10,030 patients.

Self-supervised pipeline can learn to segment ultrasound.

After confirming reports^{26,41} that chamber measurements derived from computer vision alone correlate poorly with clinical measures (Fig. S2, initial steps in Fig.2), we developed the supervised learning pipeline (Fig. 1) described above and in the Methods. Figures 2A-2L show examples of segmentation performance through successive steps in the pipeline for all three views, showing that subsequent steps in the pipeline can correct initial errors, even on images across a range of qualities and pathologies.

To demonstrate incremental impact of each step of the pipeline on prediction performance and generalizability, segmentations from intermediate steps of the pipeline were compared to clinical area measurements on images from the validation dataset (Fig. 2L-O). The r^2 on chamber areas ranged from 0.06-0.22 when using initial weak labels compared to 0.53-0.81 using the full pipeline. Bias and LOA similarly improved with successive training steps.

Pipeline-derived structure and function measurements are comparable to clinical echocardiogram measurements. Pipeline-derived measurements in the all-comers dataset were compared to clinical echocardiogram measurements (Fig. 3, Table S1, Fig. S3-S4).

Left ventricle. Pearson correlations (r) between the AI pipeline and clinical echocardiogram measurements for LV end-diastolic volume (LVEDV), LV end-systolic volume (LVESV), and LV ejection fraction (LVEF) were 0.84, 0.9, and 0.81, respectively (Table S1). r^2 for these measurements were 0.70, 0.82, and 0.65; notably, the r^2 for LVEF achieved through the self-supervised AI pipeline is better than those reported from supervised learning^{8,42} (Fig. 3A-3C, Table S1). Bland-Altman bias \pm LOA (two standard deviations) for LVEDV, LVESV, and LVEF were 2.8 \pm 51mL, 5.3 \pm 31mL, and -5.3 \pm 14.6%, respectively, similar to clinician variability studies^{13,43-45} and consistent with those achieved from supervised learning^{8,42} (Fig. 3A-3C, Table S1, Fig. S3). Correlations for LV mass were lower ($r=0.75$, $r^2=0.56$), but are still similar to reported benchmarks (Fig. 3D).

Right ventricle. r^2 were 0.69 and 0.71 for RVEDA and RVESA, respectively, indicating a strong correlation⁴⁶ between the SSL pipeline and clinical measurements. r 's were 0.83 and 0.84 and bias \pm LOA was -0.86 \pm 5.4 cm², 1.61 \pm 3.9 cm² (Table S1, Fig. 3F-3G, Fig. S3).

Atria. The r^2 for left atrial volume was 0.84, showing a very strong correlation⁴⁶. bias \pm LOA was -0.14 \pm 20mL, consistent with clinical inter-observer bias and with supervised learning performance reported in the literature^{8,43} (Fig 3E). Right atrial volume r^2 was 0.76 and bias \pm LOA between SSL and clinical measurements was -2.1 \pm 21mL (Fig. 3H).

Normal vs abnormal. For further clinical context, the above measurements were indexed to body surface area where applicable and binned as normal or abnormal according to reference guidelines^{3,47}. Accuracies and Cohen's kappa values are presented in **Error! Reference source not found.**, Table S1 and Figure S4. Accuracy ranged from 0.71 for LV mass to 0.97 for LVEF. Kappa values ranged from 0.54 to 0.79 showing a moderate to substantial agreement⁴⁶ between AI pipeline and clinical echocardiogram measurements. LV mass and RVESA were the exceptions, where kappa values were only fair.

Taken together, measurements derived from self-supervised learning performed similarly to clinical inter- and intra-observer variability and to measurements derived from supervised deep learning.

Self-supervised segmentation and clinical echo correlate similarly to CMR gold standard.

Compared to all-comers, the CMR subset is younger, more male, and has more LV dysfunction (Table 1). Also, due to the nature of different clinical imaging protocols, CMR studies did not include measurements for all chambers. Despite this, correlations between SSL-derived measurements and CMR were similar to those of clinical echo measurements and CMR (Fig. 3, Table S1).

Comparison of clinical echocardiogram measurements to CMR served as a benchmark. r^2 ranged from 0.67-0.76 for LV size and function. Bland-Altman bias \pm LOAs were $-60\pm 96\text{mL}$, $-34\pm 83\text{mL}$, $2.5\pm 20\%$, for LVEDV, LVESV, LVEF. These levels of agreement are similar to those reported in the literature^{13,48}, with echocardiography systematically underestimating LV systolic and diastolic size. LV mass showed poorer correlation with r^2 and Bias \pm LOA of 0.32 and $11\pm 169\text{g}$. Comparing SSL-derived measurements to those from CMR showed similar to slightly worse correlations and similar limits of agreement (Fig. 3). r^2 for LV size and function ranged from 0.60 to 0.72. Bias \pm LOA for LVEDV, LVESV, LVEF, and LV mass were $-57\pm 108\text{mL}$, $-30\pm 94\text{mL}$, $-1.5\pm 22\%$, and $20\pm 159\text{g}$, respectively (Fig. 3D, Table S1, Fig. S3). As with the benchmark comparison of clinical echocardiography to CMR, LV mass from the SSL pipeline showed worse performance with $r^2 = 0.32$.

When indexed and binarized into normal vs. abnormal values, accuracies and kappas for LVEDV, LVESV, LVEF, and LV mass were the same or slightly better for the SSL pipeline than the clinical benchmark (Fig. 3A-3D, Sig. S4). Moreover, measurements derived from the SSL pipeline are more sensitive for abnormal biometrics (Fig. S4).

AI pipeline performs well on external data.

The external dataset offered the opportunity to calculate Dice scores between SSL-predicted segmentation and manual tracings of the left ventricle, as well as comparison of LV function using estimations for LVEF (see Methods).

The average Dice score comparing SSL to manual tracing was 0.89 (95% CI [0.89]), representing good agreement. (For comparison, inter-observer variability in Dice scores on manual annotations of the left ventricle can range from 0.82-0.93⁴⁹.)

With no A2C images available, we estimated LVEF using A4C images alone. When binarized by normal vs. abnormal, accuracy for LVEF was 0.79 compared to estimates provided for the external dataset. Notably, the SSL pipeline predicted segmentations for all four chambers, but labels were not available for LA, RV, or RA for performance evaluation.

Discussion

Segmentation is a global, critical, and challenging task in ultrasound—exactly the sort of task that deep learning promises to help with. However, the noisy ultrasound modality presents a conundrum: it is recalcitrant to self-supervised learning, and yet supervised learning would require even more burdensome manual labeling. We solve this problem by developing a pipeline for self-supervised¹ segmentation of cardiac chambers from echocardiograms without any manual annotation, to our knowledge the first achievement of its kind. Self-supervised learning can facilitate the development medical foundation models without overburdening clinicians. To demonstrate rigor^{40,50,51}, we tested on large internal and external datasets—over 40 times the size of the training dataset. Furthermore, the all-comers dataset represented a full range of clinical characteristics and real-world image qualities—no image was excluded due to quality or pathology—making the fact that SSL pipeline’s comparison to clinical measurements all the more impressive. We benchmarked our results against available measurements at several levels, including clinical echo measurements, CMR, inter-observer variability reported in the clinical literature, and supervised learning.

The scaling implications for self-supervised segmentation in echocardiography are clear. For our 450 training echocardiograms alone, we estimate (based on timed manual annotations of a small sample) that manually labeling all chambers in all three views would have taken a human 1,664 hours. The fact that both internal and external datasets are missing many segmentations both systematically (e.g., right heart, left atrium) and randomly are testament to the laborious nature of segmentation in clinical practice as well. While manual segmentation scales poorly with each additional chamber, our human-label free pipeline is able to segment all chambers in an image simultaneously: for example, we predicted segments for all four chambers in the external dataset even though it only had left ventricular manual labels. Self-supervised segmentation in ultrasound has the potential to impute segmentations for large datasets, with beat-to-beat and even frame-to-frame granularity as previously demonstrated³⁹, for both clinical and research use. In this manuscript, we focused on measurements we could validate against available clinical measurements from our dataset, but a range of additional measurements are immediately possible. Scaling to segmentations of other anatomic structures, other views, and other types of ultrasounds are also feasible relatively quickly, using the same techniques demonstrated here.

In achieving self-supervised segmentation for echocardiograms, we demonstrate the effect of combining several deep learning techniques with traditional computer vision and with clinical spatial and geometric information. Computer vision preprocessing choices were driven by the physics of ultrasound imaging. We used two types of neural networks—segmentation networks that are known to detect ‘textures,’ as well as edge-detection networks to strengthen ultrasound’s noisy boundaries—to obtain better predictive performance than could be obtained from either one alone. Using a sequence of neural networks with leveraging early stopping and self-learning allowed each successive step in the pipeline benefitted from more data with cleaner labels. Even a label as weak as a Hough circle for the SAX view, a reasonable LV segmentation was recovered, demonstrating the power of this approach. Finally, we found that using spatial modeling information in our pipeline as clinical domain knowledge improved performance⁵². Despite promising results, the SSL pipeline has also some limitations. While bias±LOA from the pipeline was comparable to clinical and supervised ML benchmarks, an ideal pipeline would have even tighter limits of agreement. From a practical standpoint, manual supervision of a strategically chosen²⁹ subset of images to improve on the results presented here; however, the purpose of this study was to demonstrate the potential of a completely human-label-free approach.

While not a function of the SSL pipeline itself, selection of image frames to serve as systolic and diastolic timepoints in real-world ultrasound clips is also a potential source of error (and an open problem which affects supervised segmentation as well⁸). If a clinician chose different systolic and diastolic frames for measurement, the final clinical measurement could differ from the AI pipeline even if frame-for-frame segmentations are highly concordant (as shown in the external dataset).

Additionally, repeated manual measurements on our echo data from multiple observers could better define the gold-standard echo measurement and reduce the potential effect of inter-observer measurement error on the clinical gold-standard, but doing this for thousands of test echocardiograms was not feasible within the scope of this study.

In summary, self-supervised segmentation of ultrasound represents a paradigm shift in how, rather than laboring to provide labels for data-hungry machine learning models, we can get machine learning to work for us efficiently, robustly, and scalably even for challenging imaging modalities, in order to solve important problems in cardiology and beyond.

Tables

Table 1. Study population demographics.

Characteristics	Training & validation set (n=450)		Holdout test set (n=8,393)				External test set (n=10,030)	
			All-comers (n=8,393)		Subset with CMR (n=553)			
	Nb present	N (%)	Nb present	N (%)	Nb present	N (%)	Nb present	N (%)
Female	450	220 (49%)	8393	4204 (50%)	553	236 (43%)	10,030	4885 (48%)
LV Ejection Fraction <35%	402	20 (5%)	5544	468 (6%)	480	72 (15%)	10,030	948 (8%)
LV Ejection Fraction abnormal (qualitative)	447	89 (20%)	1162	412 (35%)	461	228 (49%)	-	-
LV Diastology abnormal	333	184 (55%)	798	427 (54%)	316	142 (46%)	-	-
LV Size abnormal	438	115 (26%)	1125	322 (29%)	444	155 (35%)	-	-
LV Mass abnormal	381	129 (34%)	983	298 (30%)	363	133 (37%)	-	-
Measurements	Nb present	avg±std (range)	Nb present	avg±std (range)	Nb present	avg±std (range)	Nb present	avg±std
Age, years	450	58±17 (20-90)	8393	61±17 (15-120)	553	50±16 (19-88)	10,030	68±21
BSA, m ²	450	1.88±0.28 (1.1-2.9)	8393	1.85±0.26 (0.7-4.3)	553	1.89±0.25 (1.2-3.1)	-	-
LV Ejection Fraction, %	402	61±12 (8-83)	5665	60±12 (4-89)	485	55±16 (10-86)	10,030	55.7±12.5
LV End Diastolic Volume Index, mL/m ²	402	56±23 (19-211)	5665	54±23 (10-244)	485	64±29 (10-234)	10,030	91.0±45.7*
LV End Systolic Volume Index, mL/m ²	402	24±19 (5-172)	5665	23±19 (3-203)	485	31±25 (3-189)	10,030	43.3±34.5*
LV Mass Index, g/m ²	335	91±34 (34-290)	5138	87±29 (27-293)	49	95±35 (35-255)	-	-
LA Volume Index, mL/m ²	275	31±14 (10-98)	2177	32±14 (8-202)	-	-	-	-
RA Volume, mL	-	-	1022	22±13 (4-143)	-	-	-	-
RV End Diastolic Area, cm ²	-	-	381	17±5 (7-40)	-	-	-	-
RV End Systolic Area, cm ²	-	-	381	9±4 (3-28)	-	-	-	-

Nb present = number of patients for whom each measurement was available. LV = left ventricle, LA = left atrium, RV = right ventricle, RA = right atrium, BSA = body surface area.

*Values are not indexed by BSA.

Figure Legends

Figure 1. Overview of the self-supervised segmentation pipeline. (A) A2C segmentation. (A1) Initial weak label creation using computer vision. (A2) Semantic segmentation training includes initial training with early learning (A2-1) and self-learning (A2-2) to arrive at a final trained model used to run inference on test data. (B) A4C segmentation. (B1) Initial weak label creation from inference using the A2C final model from (A), resulting in predictions of two “LA” and two “LV” chambers per image. (B2) Predictions from B1 were reassigned four chamber labels, and clinically-guided morphological operations were performed to stretch the RV apex (white dot) to known correlations of RV and LV length (white box). Early learning (B2-1) and self-learning (B2-1) were then performed to arrive at the final A4C model. (C) SAX segmentation. (C1) Initial weak labels were generated through Hough circle detection and (C2) a holistic edge detection (HED) network was trained (early learning). (C3) The prediction from C2 was then filled in and used as a label to train a UNet. Dilation and erosion were applied to the UNet prediction to create labels of the epicardial and endocardial areas. A second UNet was trained with these labels on the same images (self-learning), resulting in the final model. (D) Clinical calculations. Predictions from A2, B2, and C3 were used to compute chamber dimensions, areas, volumes, and Dice scores on all-comers and external test datasets, respectively. LV = left ventricle (red), LA = left atrium (light blue), RV = right ventricle (dark blue), RA = right atrium (pink), HED = holistically nested edge detection, A2C = apical 2-chamber, A4C = apical 4-chamber, SAX = short-axis mid.

Figure 2. Examples of segmentation and measurement improvement through successive steps of the SSL pipeline. Evolution of segmentation for several examples for A2C (A-D), A4C (E-H), and SAX (I-L). (A) shows a typical good-quality A2C image: the initial weak label (step A1) segments the chambers poorly but are corrected through successive steps of the pipeline to final prediction (step A2). The pipeline performs well even with left atrial enlargement in a technically difficult image (B), an image where LV contrast (white arrow) obscures the LV lumen (C), and an image with a large LA mass (blue arrowheads) prolapses into the LV (D). (E) shows a typical good-quality A4C image and its segmentation from the initial weak label (step B1) to final prediction (step B2). In (F), a filling defect from an LV thrombus (white arrow) was still present in the final segmentation. In (G), segmentation performs well despite presence of a

pericardial effusion (blue arrowheads). In (H), segmentation performs despite RA and RV enlargement and septal flattening due to pulmonary hypertension. (I) shows a typical good-quality SAX image: the initial weak label (step C1) is a simple circle, but segmentations are built up through successive steps of the pipeline to final prediction (step C3). In (J), final segmentation prediction is reasonable despite a slightly off-axis SAX. In (K), segmentation performs despite pulmonary hypertension and septal flattening, but the true degree of septal flattening is blunted in the final prediction. In (L), segmentation performs poorly due to a technically difficult image with dropout in the area of the septum, but still recovers a final prediction despite no prediction in step C2. (M)-(P) show area measurements calculated from segmentations at different steps in the pipeline, using images from the validation dataset. r^2 and Bland-Altman bias \pm LOA comparing these measurements with clinical echocardiogram measurements improve across successive steps in the pipeline. Light blue, limits of agreement (two standard deviations); medium blue, one standard deviation. A2C = apical 2-chamber, LV = left ventricle, LA = left atrium, LOA = limits of agreement.

Figure 3. Comparison of clinical and SSL-derived chamber measurements for (A) LV end-diastolic volume (LVEDV), (B) LV end-systolic volume (LVESV), (C) LV ejection fraction (LVEF), (D) LV mass, (E) LA volume, (F) RV end-diastolic area (RVEDA), (G) RV end-systolic area (RVESA), and (H) RA volume. The datasets being compared are listed on the left, along with the number of datapoints in parentheses. Open (white) circles indicate intra-modality comparisons (echocardiography). Pink circles indicate comparisons across modality (to CMR). Light blue bars indicate Bland-Altman limits of agreement (LOA; two standard deviations); darker blue bars indicate one standard deviation. Black asterisk in (D) indicates an assumed Bland-Altman bias, as only LOA was reported. Vertical shading in the kappa comparison plots indicates ranges for poor (purple), fair (blue), moderate (teal), good (green), and excellent (yellow) agreement. Clinical intra-observer references include Jacobs et al 2006 for LVEDV, LVESV, and LVEF¹⁵; Crowley et al 2016 for LV mass⁵³; and Mihaila et al 2017 for LA volume. Supervised learning references include Ghorbani et al 2020⁴² and Zhang et al 2018⁸.

Acknowledgements: We thank the patients, sonographers and clinicians whose work created the datasets used to develop and test this pipeline.

Sources of Funding: D.F. and R.A. were supported by the National Institutes of Health (R01HL150394) to R.A. R.A. is additionally supported by the Department of Defense (PR181763) and the Chan Zuckerberg Biohub.

Disclosures: None relevant.

Independent data access and analysis: R.A. and D.F. had full access to all the data in the study and takes responsibility for its integrity and the data analysis.

Contributions: R.A. and D.F. conceived of the study. D.F. performed data analysis with input from R.A. Z.S. performed data acquisition with input from R.A. R.A. and D.F. wrote the manuscript with input from Z.S.

Supplemental Material: Supplemental Methods; Tables S1–S2; Figure S1-S4

References

1. Strickland E. Yann Lecun: Ai doesn't need our supervision. IEEE Spectrum 2022.
2. Douglas PS, Garcia MJ, Haines DE, Lai WW, Manning WJ, Patel AR, et al. ACCF/ASE/AHA/ASNC/HFSA/HRS/SCAI/SCCM/SCCT/SCMR 2011 Appropriate Use Criteria for Echocardiography. *J Am Coll Cardiol Img* 2011;57:1126–1166. doi:10.1016/j.jacc.2010.11.002.
3. Lang RM, Badano LP, Mor-Avi V, Afilalo J, Armstrong A, Ernande L, et al. Recommendations for Cardiac Chamber Quantification by Echocardiography in Adults: An Update from the American Society of Echocardiography and the European Association of Cardiovascular Imaging. *Journal of the American Society of Echocardiography* 2015;28:1-39.e14. doi:10.1016/j.echo.2014.10.003.
4. Thavendiranathan P, Popović ZB, Flamm SD, Dahiya A, Grimm RA, Marwick TH. Improved Interobserver Variability and Accuracy of Echocardiographic Visual Left Ventricular Ejection Fraction Assessment through a Self-Directed Learning Program Using Cardiac Magnetic Resonance Images. *Journal of the American Society of Echocardiography* 2013;26:1267–1273. doi:10.1016/j.echo.2013.07.017.
5. Flachskampf FA, Nihoyannopoulos P. Our obsession with normal values. *Echo Res Pract* 2018;5:R17–R21. doi:10.1530/ERP-17-0082.
6. Foley TA, Radiologist, Department of Radiology, Mankad SV, Cardiologist, Anavekar NS, Cardiologist, et al. Measuring Left Ventricular Ejection Fraction – Techniques and Potential Pitfalls. *European Cardiology Review* 2012;8:108. doi:10.15420/ecr.2012.8.2.108.
7. Arnaout R, Curran L, Zhao Y, Levine JC, Chinn E, Moon-Grady AJ. An ensemble of neural networks provides expert-level prenatal detection of complex congenital heart disease. *Nat Med* 2021;27:882–891. doi:10.1038/s41591-021-01342-5.
8. Zhang J, Gajjala S, Agrawal P, Tison GH, Hallock LA, Beussink-Nelson L, et al. Fully Automated Echocardiogram Interpretation in Clinical Practice: Feasibility and Diagnostic Accuracy. *Circulation* 2018;138:1623–1635. doi:10.1161/CIRCULATIONAHA.118.034338.
9. Ouyang D, He B, Ghorbani A, Yuan N, Ebinger J, Langlotz CP, et al. Video-based AI for beat-to-beat assessment of cardiac function. *Nature* 2020;580:252–256.

10. Willeminck MJ, Koszek WA, Hardell C, Wu J, Fleischmann D, Harvey H, et al. Preparing medical imaging data for machine learning. *Radiology* 2020;295:4–15.
11. Irvin J, Rajpurkar P, Ko M, Yu Y, Ciurea-Ilcus S, Chute C, et al. Chexpert: A large chest radiograph dataset with uncertainty labels and expert comparison. *Proceedings of the AAAI conference on artificial intelligence*, vol. 33, 2019, p. 590–597.
12. Heim E, Roß T, Seitel A, März K, Stieltjes B, Eisenmann M, et al. Large-scale medical image annotation with crowd-powered algorithms. *J Med Imaging (Bellingham)* 2018;5:034002–034002. doi:10.1117/1.JMI.5.3.034002.
13. Wood PW, Choy JB, Nanda NC, Becher H. Left ventricular ejection fraction and volumes: it depends on the imaging method. *Echocardiography* 2014;31:87–100.
14. Cole GD, Dhutia NM, Shun-Shin MJ, Willson K, Harrison J, Raphael CE, et al. Defining the real-world reproducibility of visual grading of left ventricular function and visual estimation of left ventricular ejection fraction: impact of image quality, experience and accreditation. *The International Journal of Cardiovascular Imaging* 2015;31:1303–1314.
15. Jacobs LD, Salgo IS, Goonewardena S, Weinert L, Coon P, Bardo D, et al. Rapid online quantification of left ventricular volume from real-time three-dimensional echocardiographic data. *European Heart Journal* 2006;27:460–468. doi:10.1093/eurheartj/ehi666.
16. Kirillov A, Mintun E, Ravi N, Mao H, Rolland C, Gustafson L, et al. Segment Anything 2023. doi:10.48550/arXiv.2304.02643.
17. Arnaout R. ChatGPT Helped Me Write This Talk Title, but Can It Read an Echocardiogram? *Journal of the American Society of Echocardiography* 2023;0. doi:10.1016/j.echo.2023.07.007.
18. Ratner A, Bach SH, Ehrenberg H, Fries J, Wu S, Ré C. Snorkel: rapid training data creation with weak supervision. *The VLDB Journal* 2020;29:709–730. doi:10.1007/s00778-019-00552-1.
19. Zhang L, Gopalakrishnan V, Lu L, Summers RM, Moss J, Yao J. Self-learning to detect and segment cysts in lung ct images without manual annotation. *2018 IEEE 15th International Symposium on Biomedical Imaging (ISBI 2018)*, IEEE; 2018, p. 1100–1103.
20. Jing L, Tian Y. Self-Supervised Visual Feature Learning With Deep Neural Networks: A Survey. *IEEE Trans Pattern Anal Mach Intell* 2021;43:4037–4058. doi:10.1109/TPAMI.2020.2992393.

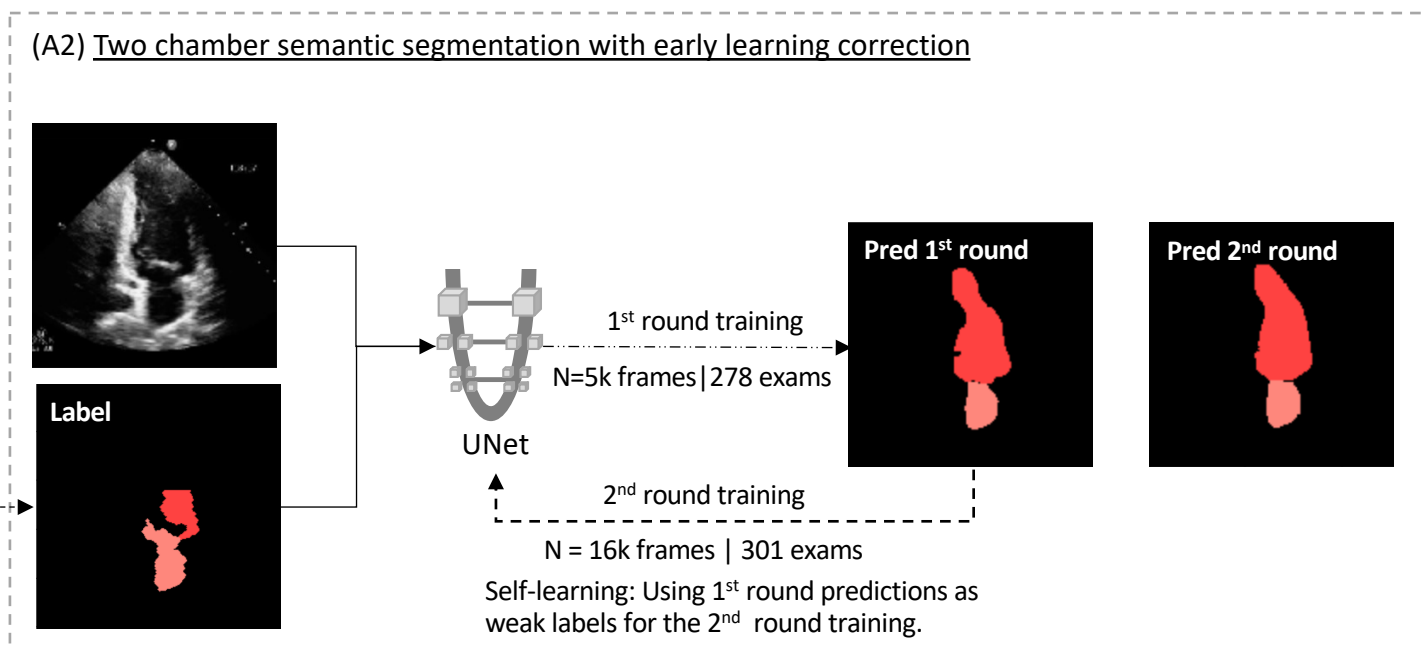
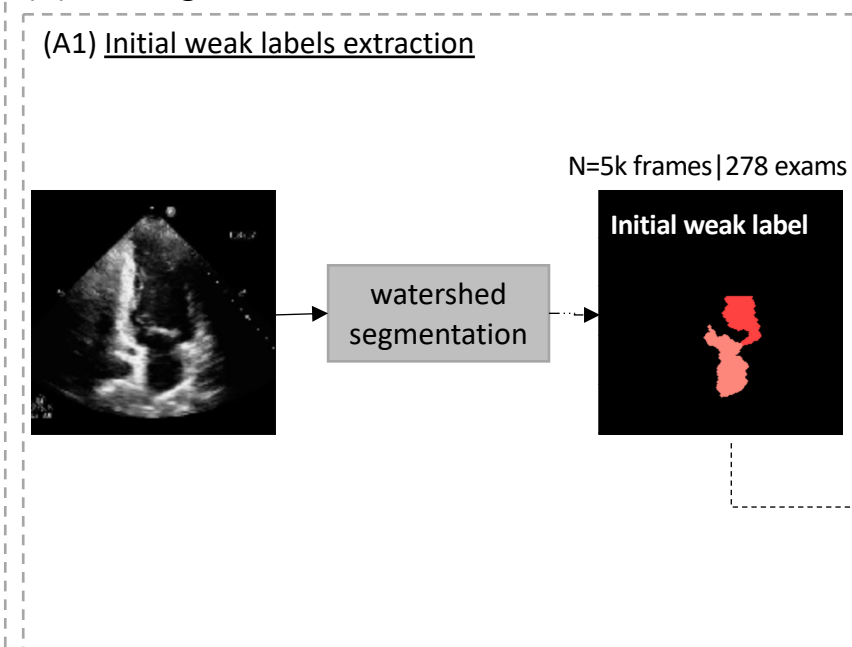
21. Krishnan R, Rajpurkar P, Topol EJ. Self-supervised learning in medicine and healthcare. *Nat Biomed Eng* 2022;6:1346–1352. doi:10.1038/s41551-022-00914-1.
22. Ghosh S, Das N, Das I, Maulik U. Understanding deep learning techniques for image segmentation. *ACM Computing Surveys (CSUR)* 2019;52:1–35.
23. Minaee S, Boykov YY, Porikli F, Plaza AJ, Kehtarnavaz N, Terzopoulos D. Image segmentation using deep learning: A survey. *IEEE Transactions on Pattern Analysis and Machine Intelligence* 2021.
24. Siddique N, Paheding S, Elkin CP, Devabhaktuni V. U-net and its variants for medical image segmentation: A review of theory and applications. *IEEE Access* 2021.
25. Carneiro G, Nascimento JC, Freitas A. The segmentation of the left ventricle of the heart from ultrasound data using deep learning architectures and derivative-based search methods. *IEEE Transactions on Image Processing* 2011;21:968–982.
26. Tavakoli V, Amini AA. A survey of shaped-based registration and segmentation techniques for cardiac images. *Computer Vision and Image Understanding* 2013;117:966–989.
27. Mazaheri S, Sulaiman PSB, Wirza R, Khalid F, Kadiman S, Dimon MZ, et al. Echocardiography image segmentation: A survey. 2013 International Conference on Advanced Computer Science Applications and Technologies, IEEE; 2013, p. 327–332.
28. Madani A, Arnaout R, Mofrad M, Arnaout R. Fast and accurate view classification of echocardiograms using deep learning. *Npj Digital Med* 2018;1:6. doi:10.1038/s41746-017-0013-1.
29. Chinn E, Arora R, Arnaout R, Arnaout R. ENRICHing medical imaging training sets enables more efficient machine learning. *J Am Med Inform Assoc* 2023:ocad055. doi:10.1093/jamia/ocad055.
30. Ronneberger O, Fischer P, Brox T. U-Net: Convolutional Networks for Biomedical Image Segmentation. In: Navab N, Hornegger J, Wells WM, Frangi AF, editors. *Medical Image Computing and Computer-Assisted Intervention – MICCAI 2015*, Cham: Springer International Publishing; 2015, p. 234–241. doi:10.1007/978-3-319-24574-4_28.
31. Xie S, Tu Z. Holistically-Nested Edge Detection 2015. doi:10.48550/arXiv.1504.06375.
32. Xie S, Tu Z. Holistically-Nested Edge Detection. arXiv:150406375 [Cs] 2015.
33. Zhang C, Bengio S, Hardt M, Recht B, Vinyals O. Understanding deep learning (still) requires rethinking generalization. *Communications of the ACM* 2021;64:107–115.

34. Arpit D, Jastrzębski S, Ballas N, Krueger D, Bengio E, Kanwal MS, et al. A closer look at memorization in deep networks. *International Conference on Machine Learning*, PMLR; 2017, p. 233–242.
35. Yu S, Chen M, Zhang E, Wu J, Yu H, Yang Z, et al. Robustness study of noisy annotation in deep learning based medical image segmentation. *Phys Med Biol* 2020;65:175007. doi:10.1088/1361-6560/ab99e5.
36. Liu S, Niles-Weed J, Razavian N, Fernandez-Granda C. Early-learning regularization prevents memorization of noisy labels. *Advances in Neural Information Processing Systems* 2020;33:20331–20342.
37. Liu S, Liu K, Zhu W, Shen Y, Fernandez-Granda C. Adaptive early-learning correction for segmentation from noisy annotations. *Proceedings of the IEEE/CVF Conference on Computer Vision and Pattern Recognition*, 2022, p. 2606–2616.
38. Triguero I, García S, Herrera F. Self-labeled techniques for semi-supervised learning: taxonomy, software and empirical study. *Knowledge and Information Systems* 2015;42:245–284.
39. Arnaout R, Curran L, Chinn E, Zhao Y, Moon-Grady A. Deep-learning models improve on community-level diagnosis for common congenital heart disease lesions. *arXiv Preprint arXiv:180906993* 2018.
40. Kakarmath S, Esteva A, Arnaout R, Harvey H, Kumar S, Muse E, et al. Best practices for authors of healthcare-related artificial intelligence manuscripts. *NPJ Digit Med* 2020;3:134. doi:10.1038/s41746-020-00336-w.
41. Saini K, Dewal ML, Rohit M. Ultrasound imaging and image segmentation in the area of ultrasound: a review. *International Journal of Advanced Science and Technology* 2010;24.
42. Ghorbani A, Ouyang D, Abid A, He B, Chen JH, Harrington RA, et al. Deep learning interpretation of echocardiograms. *NPJ Digital Medicine* 2020;3:1–10.
43. Rodevand O, Bjornerheim R, Ljosland M, Maehle J, Smith HJ, Ihlen H. Left atrial volumes assessed by three- and two-dimensional echocardiography compared to MRI estimates. *The International Journal of Cardiac Imaging* 1999;15:397–410. doi:10.1023/A:1006276513186.
44. Keller A, Gopal A, King D. Left and Right Atrial Volume by Freehand Three-dimensional Echocardiography: In Vivo Validation Using Magnetic Resonance Imaging. *European Journal of Echocardiography* 2000;1:55–65. doi:10.1053/euje.2000.0010.

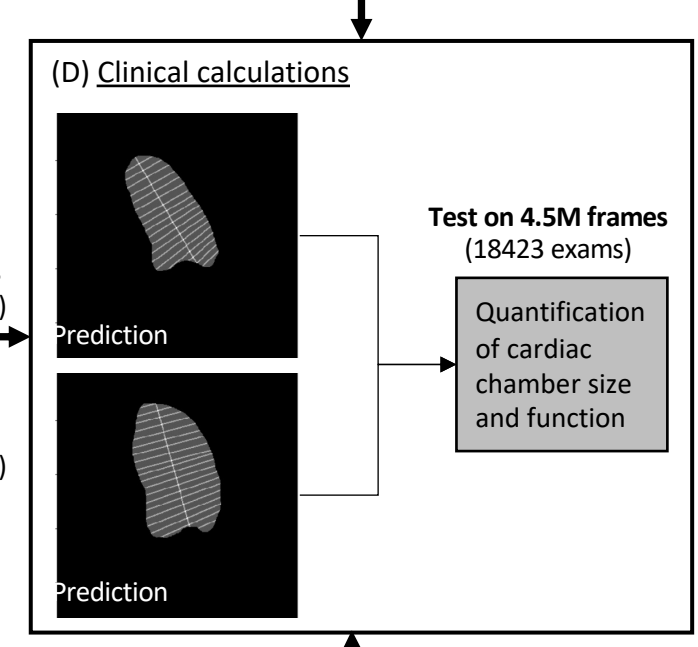
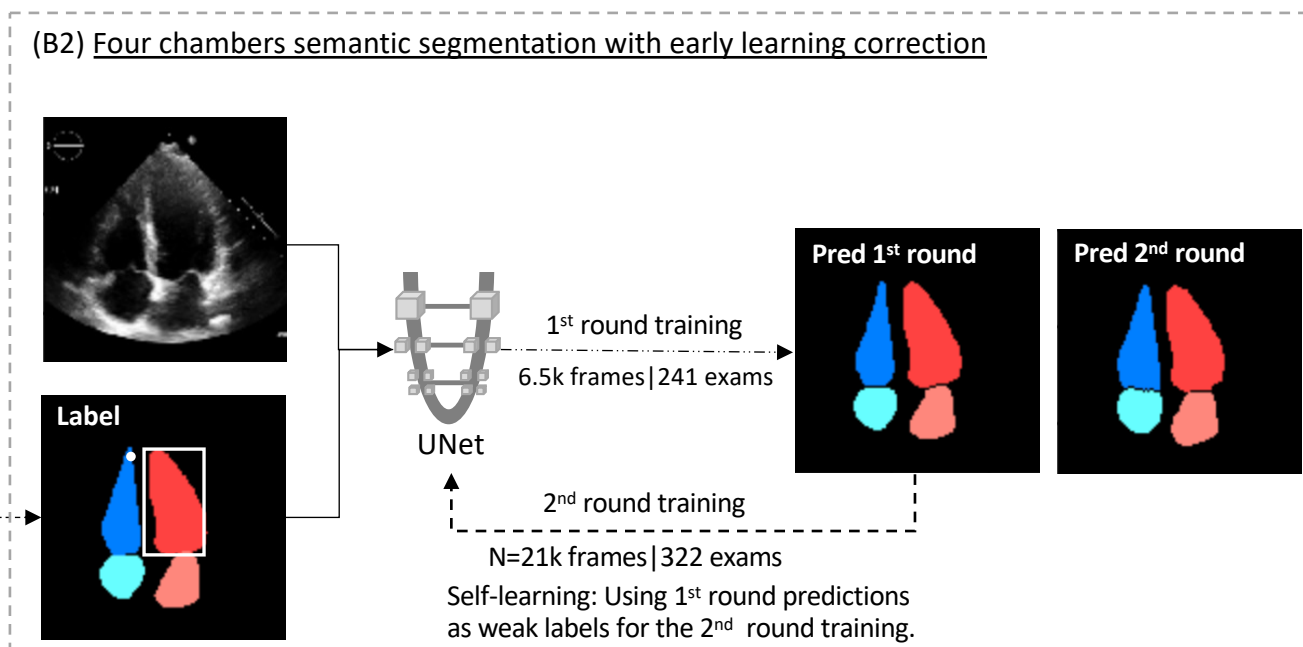
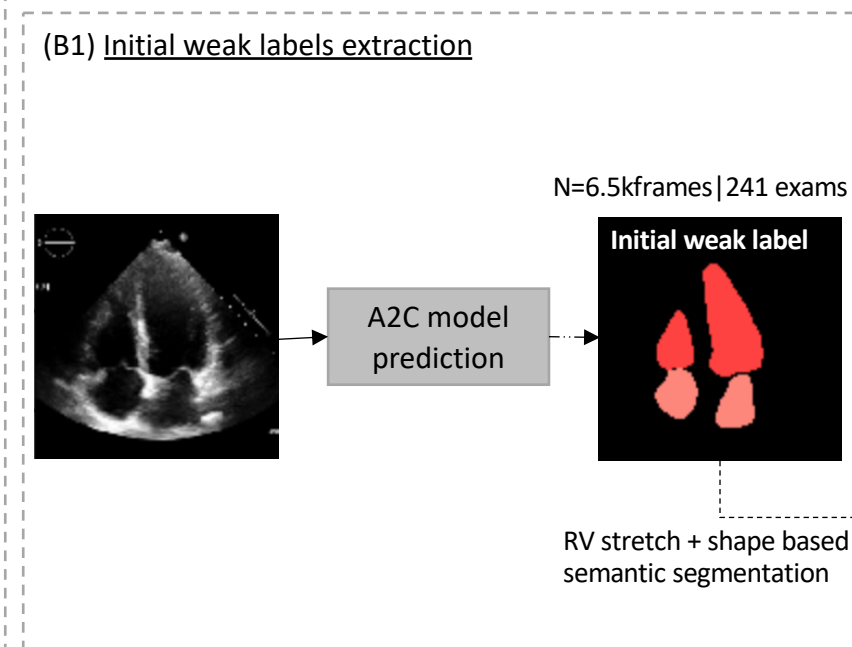
45. Mor-Avi V, Sugeng L, Weinert L, MacEneaney P, Caiani EG, Koch R, et al. Fast Measurement of Left Ventricular Mass With Real-Time Three-Dimensional Echocardiography: Comparison With Magnetic Resonance Imaging. *Circulation* 2004;110:1814–1818. doi:10.1161/01.CIR.0000142670.65971.5F.
46. Bunting KV, Steeds RP, Slater LT, Rogers JK, Gkoutos GV, Kotecha D. A practical guide to assess the reproducibility of echocardiographic measurements. *Journal of the American Society of Echocardiography* 2019;32:1505–1515.
47. Petersen SE, Khanji MY, Plein S, Lancellotti P, Bucciarelli-Ducci C. European Association of Cardiovascular Imaging expert consensus paper: a comprehensive review of cardiovascular magnetic resonance normal values of cardiac chamber size and aortic root in adults and recommendations for grading severity. *European Heart Journal - Cardiovascular Imaging* 2019;20:1321–1331. doi:10.1093/ehjci/jez232.
48. Dorosz JL, Lezotte DC, Weitzenkamp DA, Allen LA, Salcedo EE. Performance of 3-dimensional echocardiography in measuring left ventricular volumes and ejection fraction: a systematic review and meta-analysis. *J Am Coll Cardiol Img* 2012;59:1799–1808.
49. Leclerc S, Smistad E, Pedrosa J, Østvik A, Cervenansky F, Espinosa F, et al. Deep learning for segmentation using an open large-scale dataset in 2D echocardiography. *IEEE Transactions on Medical Imaging* 2019;38:2198–2210.
50. Sengupta PP, Shrestha S, Berthon B, Messas E, Donal E, Tison GH, et al. Proposed Requirements for Cardiovascular Imaging-Related Machine Learning Evaluation (PRIME): A Checklist: Reviewed by the American College of Cardiology Healthcare Innovation Council. *JACC Cardiovasc Imaging* 2020;13:2017–2035. doi:10.1016/j.jcmg.2020.07.015.
51. Norgeot B, Quer G, Beaulieu-Jones BK, Torkamani A, Dias R, Gianfrancesco M, et al. Minimum information about clinical artificial intelligence modeling: the MI-CLAIM checklist. *Nat Med* 2020;26:1320–1324. doi:10.1038/s41591-020-1041-y.
52. Isensee F, Jaeger PF, Kohl SAA, Petersen J, Maier-Hein KH. nnU-Net: a self-configuring method for deep learning-based biomedical image segmentation. *Nat Methods* 2021;18:203–211. doi:10.1038/s41592-020-01008-z.
53. Crowley AL, Yow E, Barnhart HX, Daubert MA, Bigelow R, Sullivan DC, et al. Critical Review of Current Approaches for Echocardiographic Reproducibility and Reliability

Assessment in Clinical Research. J Am Soc Echocardiogr 2016;29:1144-1154.e7.
doi:10.1016/j.echo.2016.08.006.

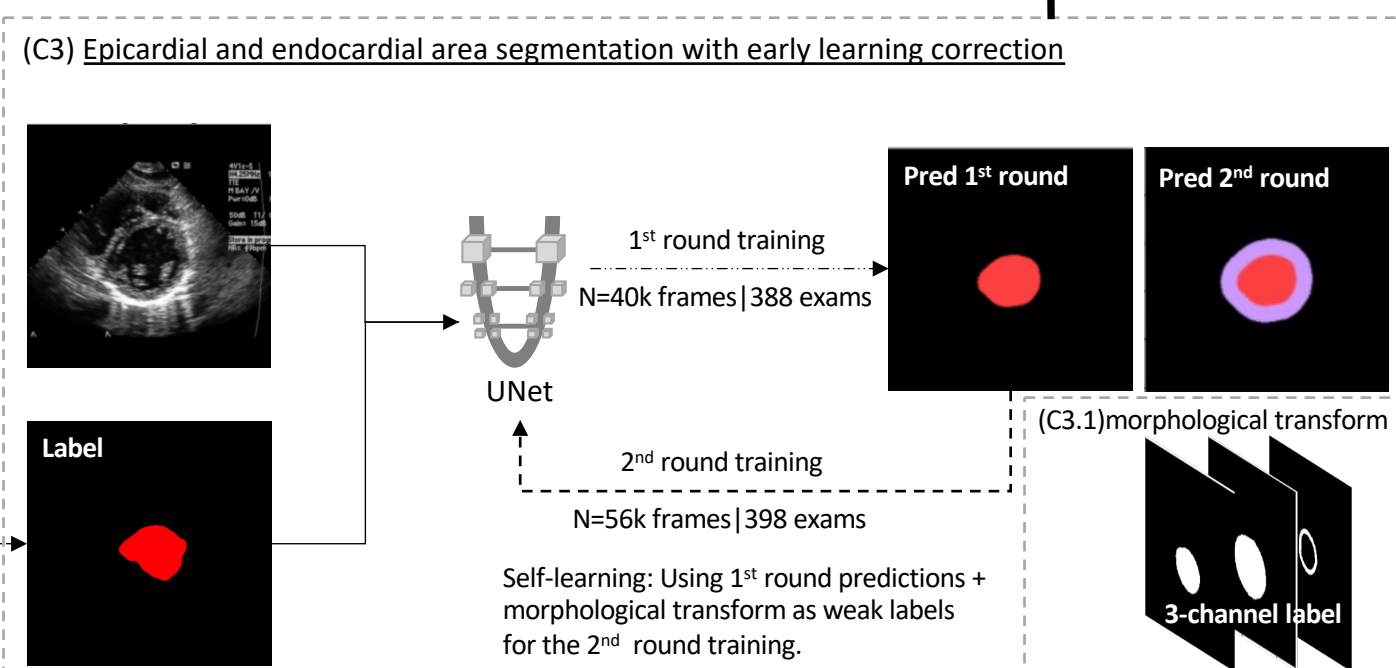
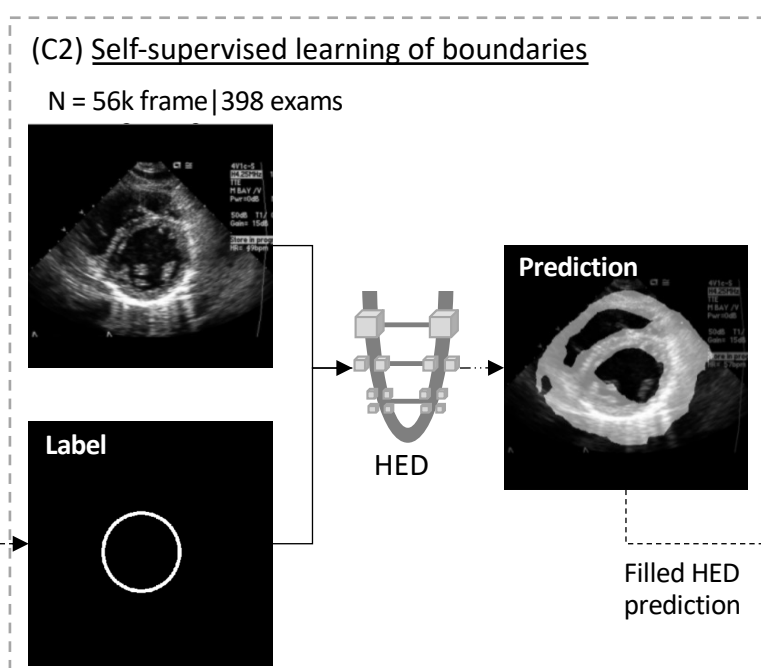
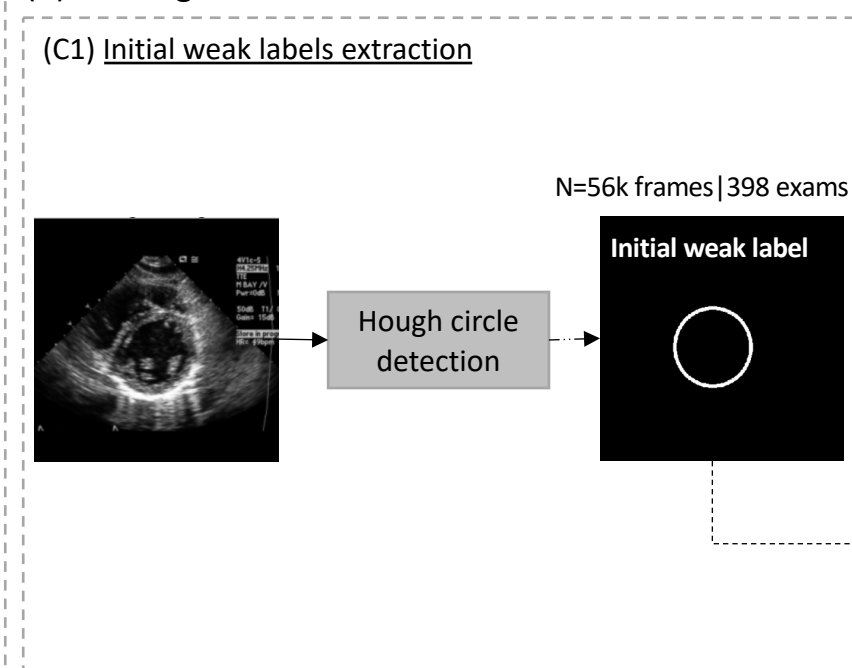
(A) A2C segmentation



(B) A4C segmentation

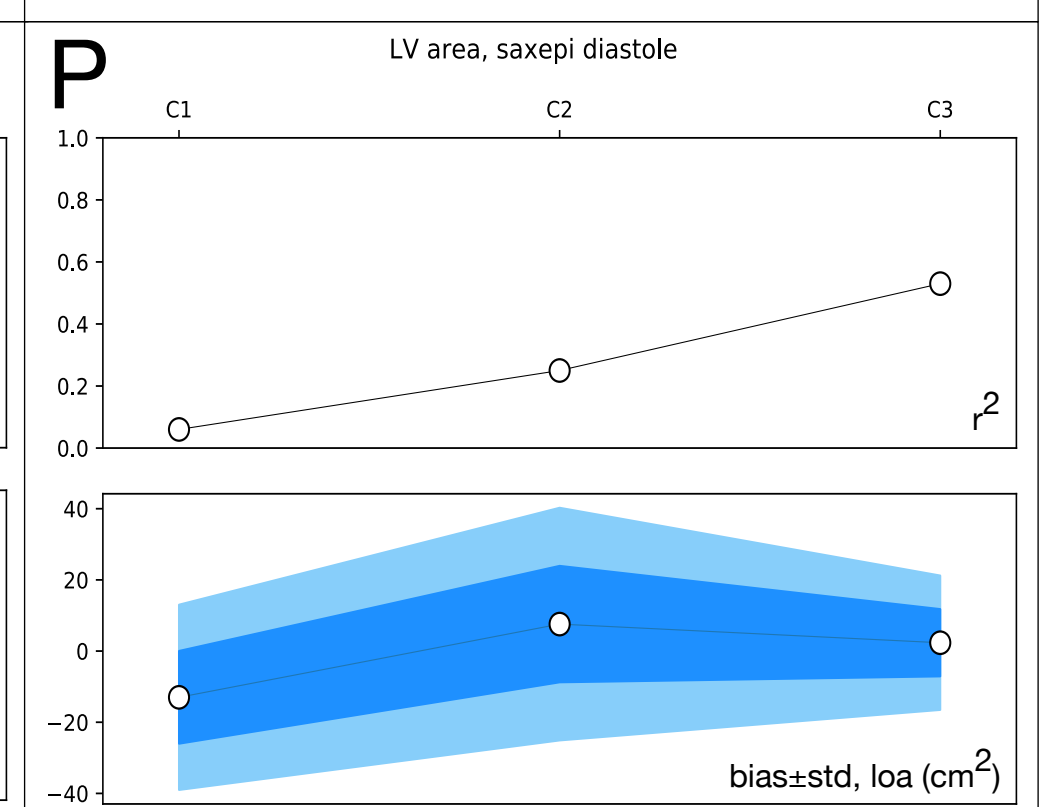
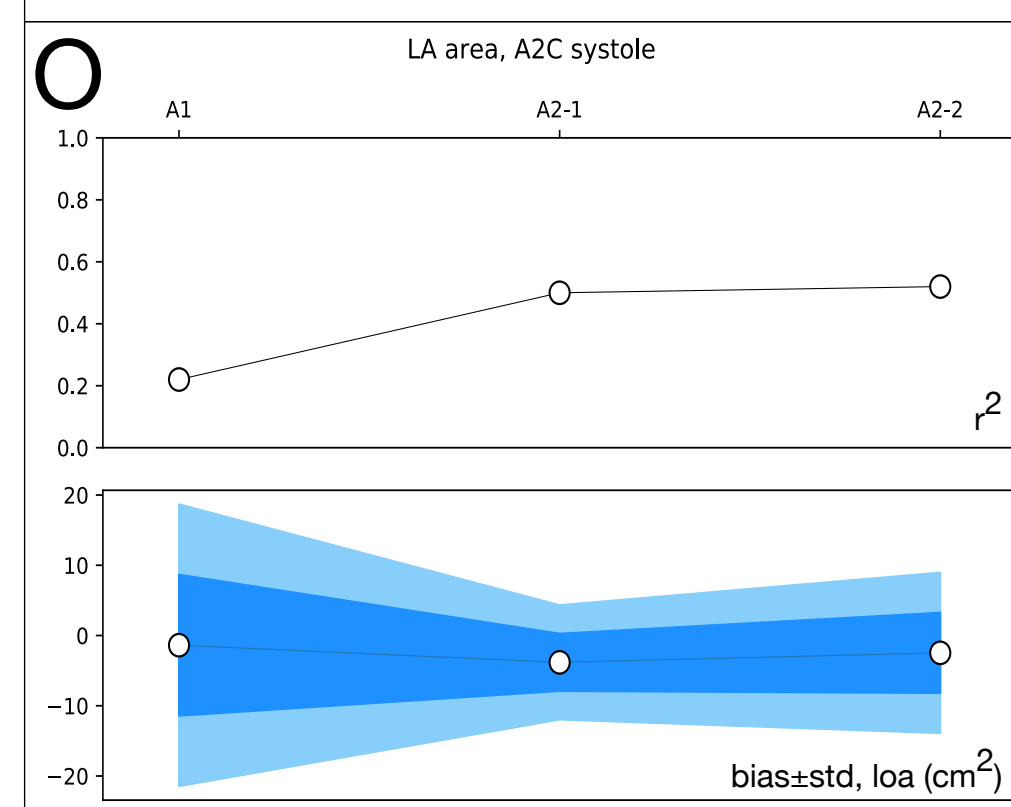
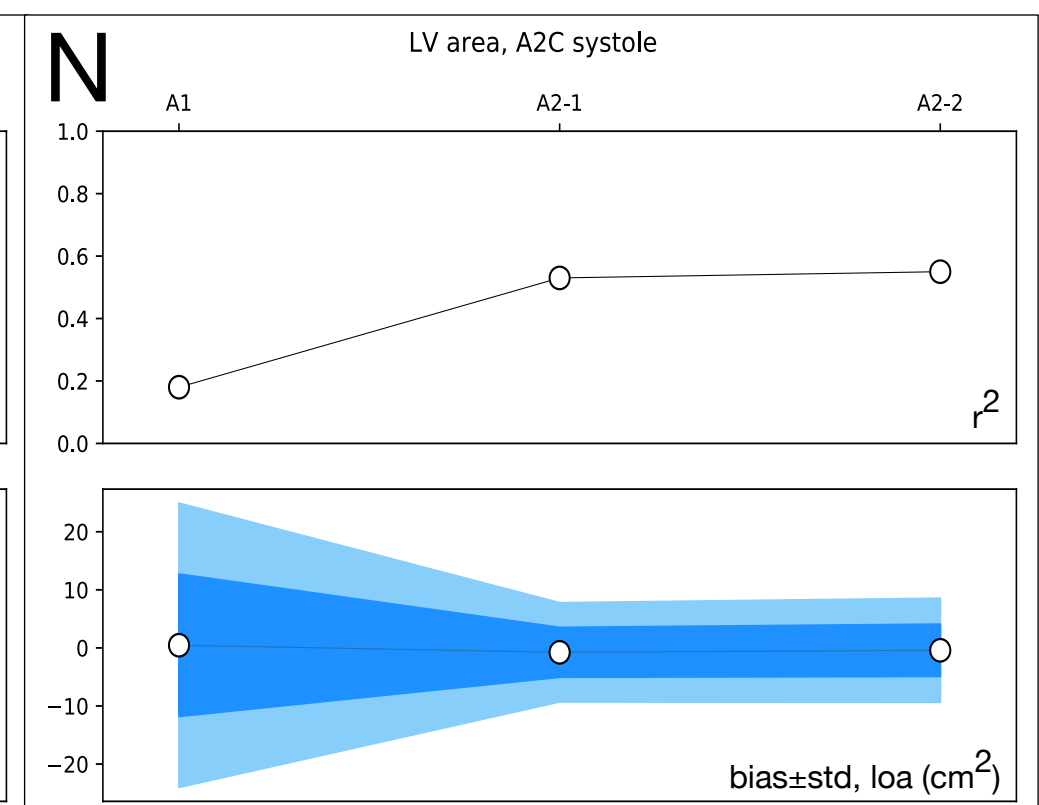
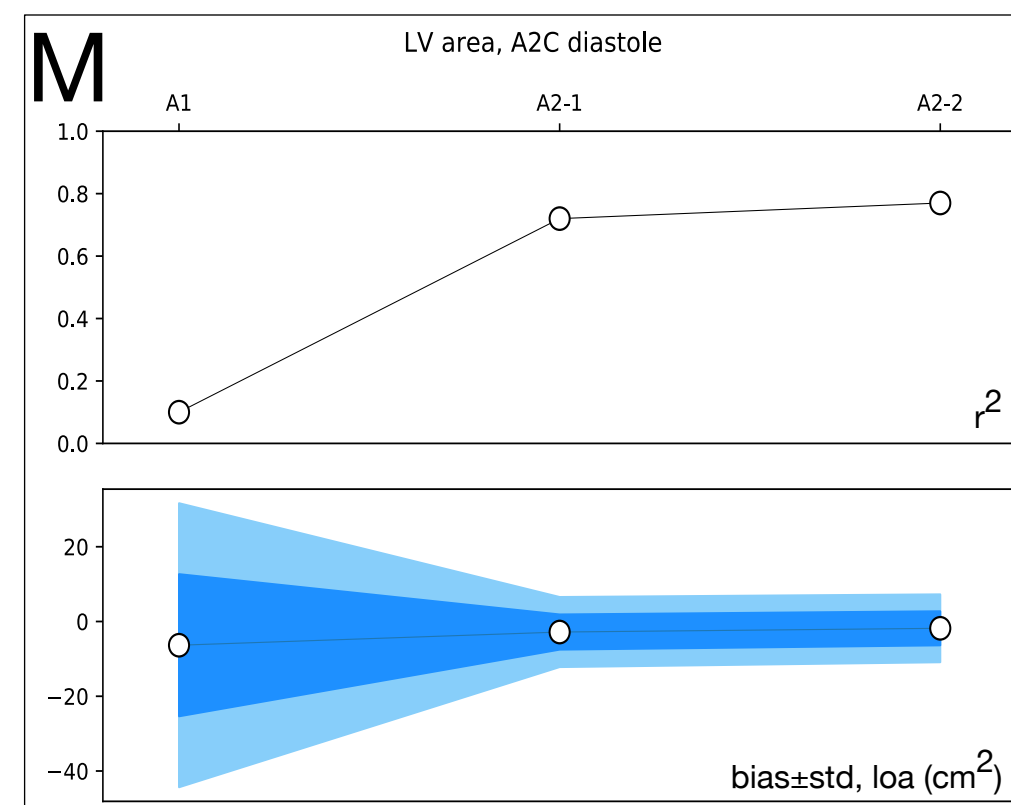
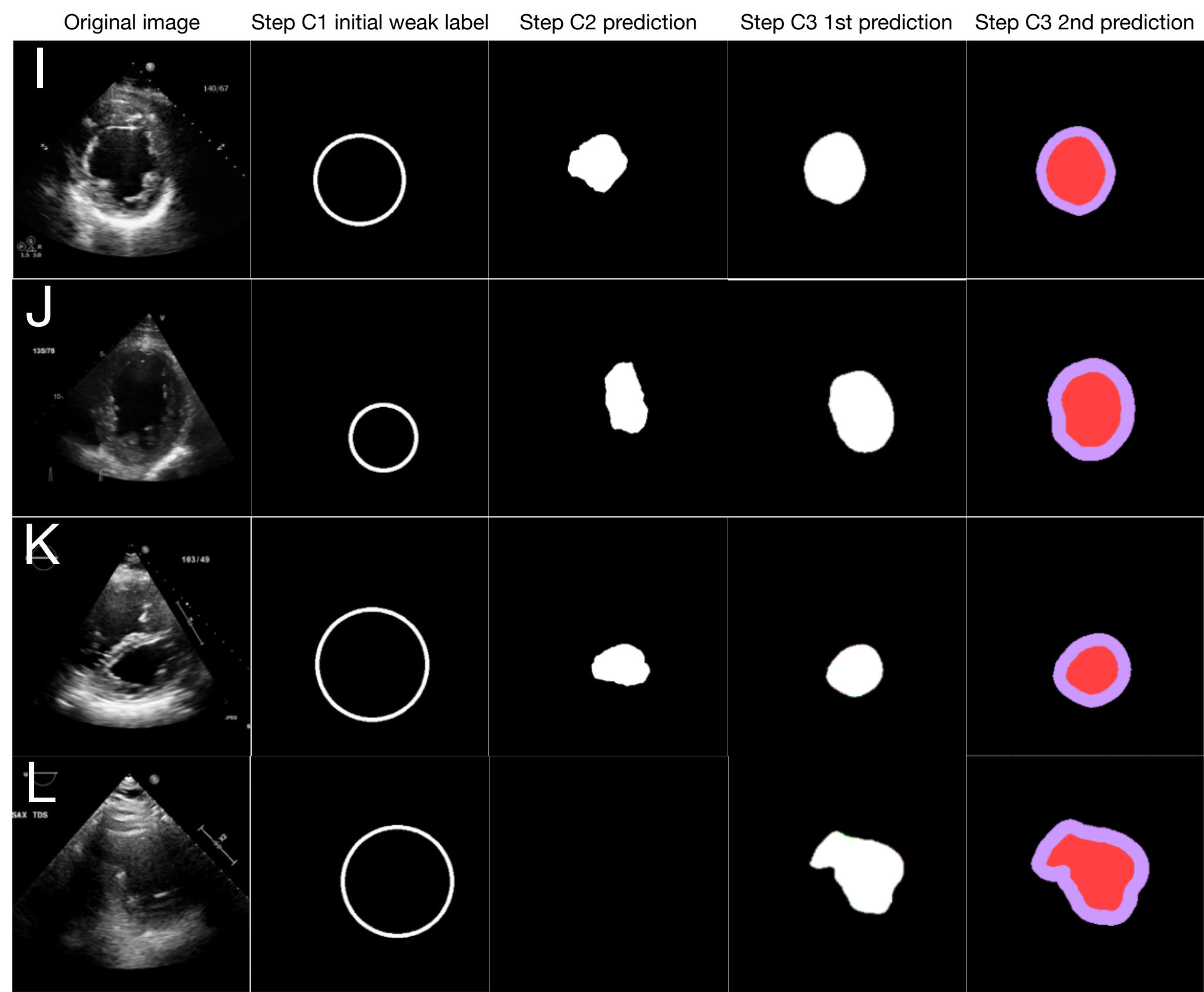
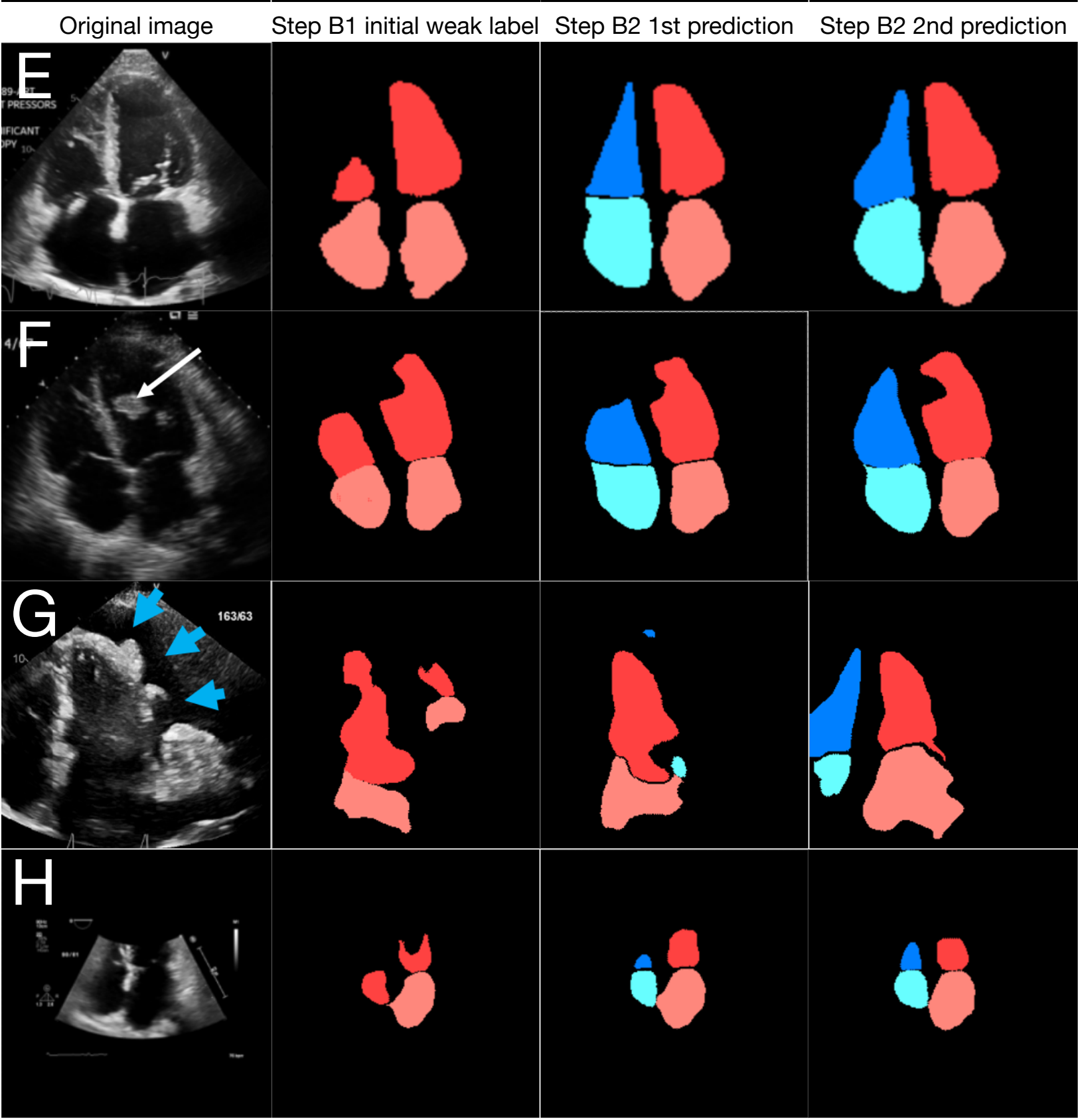
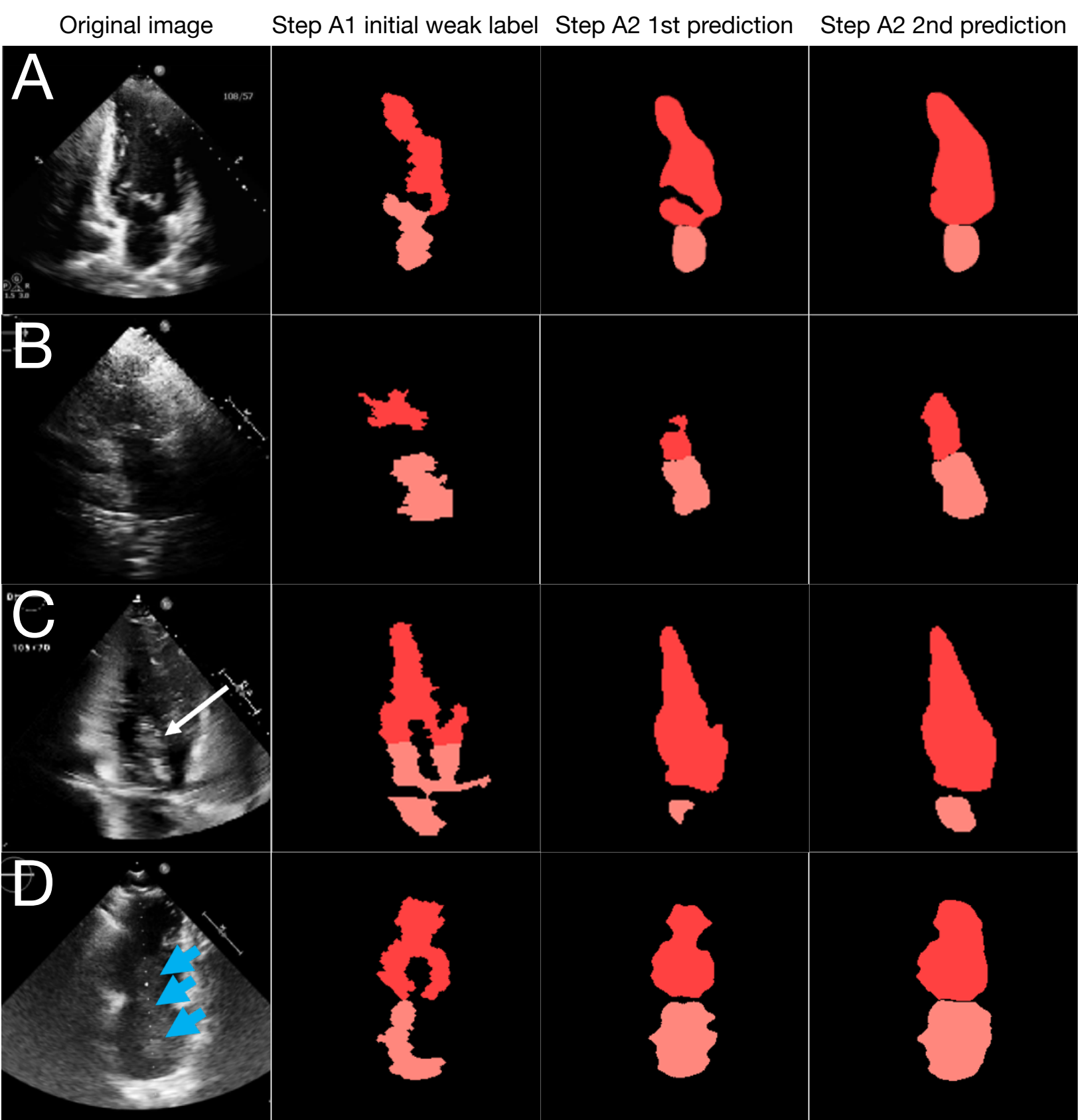


(C) SAX segmentation

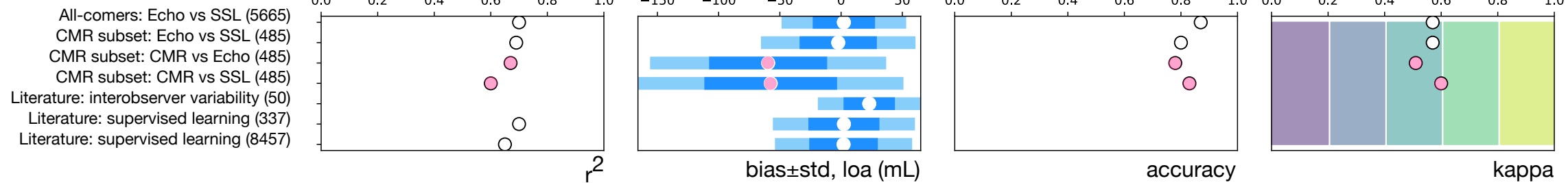


Test on TTE All-comers 1.5M frames (6981 exams)

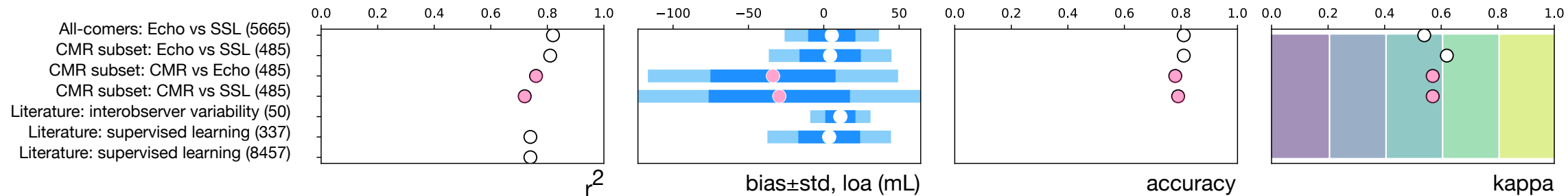
Test on TTE All-comers 1.2M frames (6507 exams)



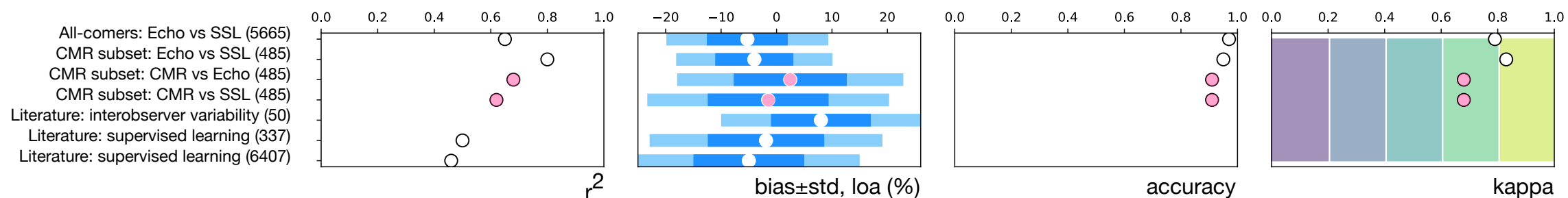
A) LVEDV



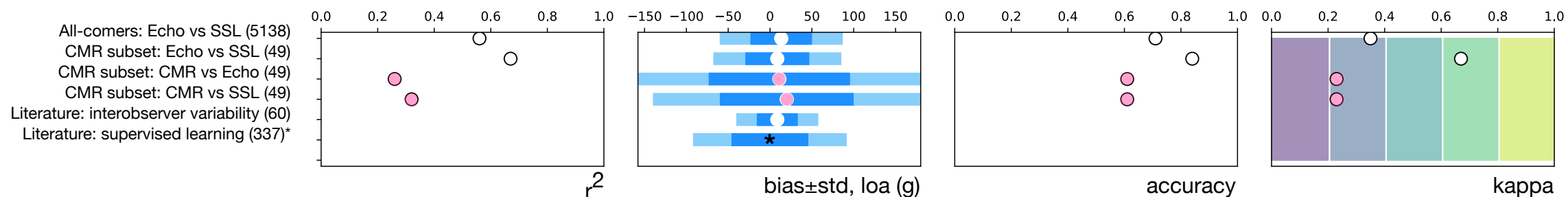
B) LVESV



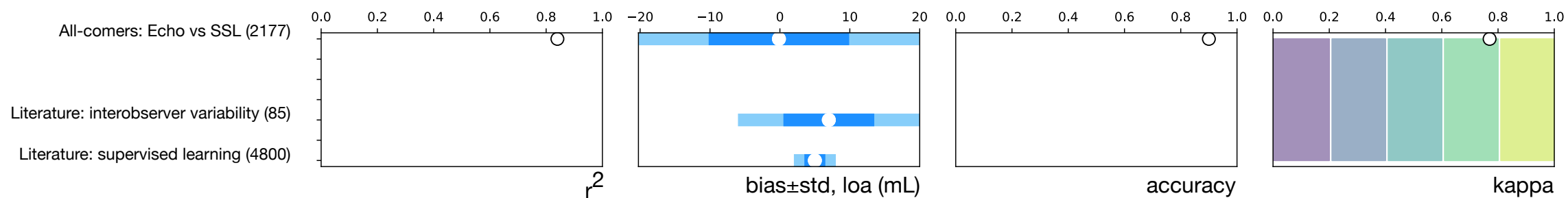
C) LVEF



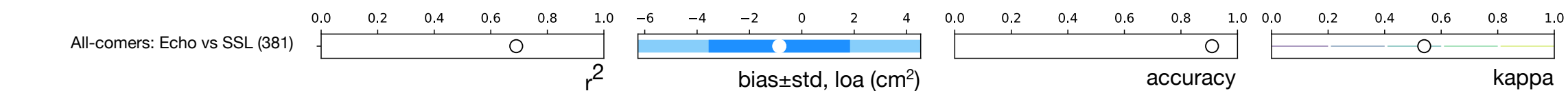
D) LV mass



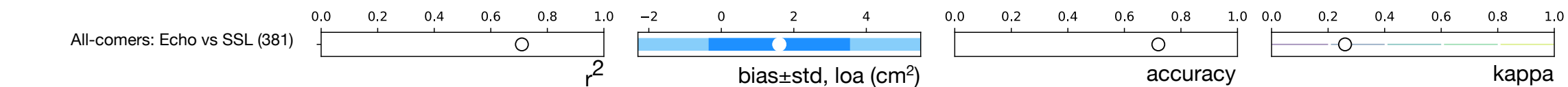
E) LA Volume



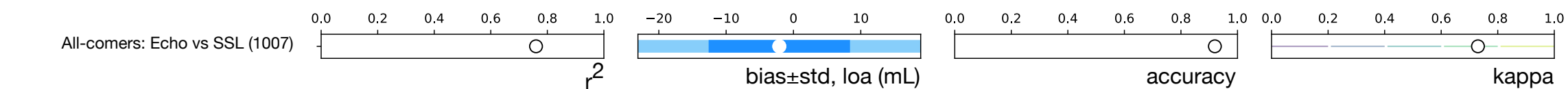
F) RVEDA



G) RVESA



H) RA Volume



Title: Self-supervised learning for label-free segmentation in cardiac ultrasound

Authors: Danielle L. Ferreira PhD, Zaynaf Salaymang RDCS, Rima Arnaout MD

Supplemental Methods

Data preprocessing and initial weak label extraction. *Initial weak label extraction, A2C view.*

A bilateral filter ($\sigma_s = 15$, $\sigma_r = 0.25$) was applied to images for speckle noise reduction¹. A Euclidean distance transform (minimum distance = 20 pixels) was then applied to propose seed points for the watershed algorithm. The watershed algorithm² was applied to create initial segments. A copy of this image was binarized (threshold = 0.1) to create a mask for the blood pool, and this mask was applied to remove watershed segments outside the blood pool. Next, connected components analysis excluded images for which the watershed algorithm failed to find at least two segments. The remaining suitable segments were labeled as ‘LA’ or ‘LV’ according to the known spatial relationship of these chambers in the A2C view. Finally, shape descriptors such as eccentricity and area were used to eliminate segments not compatible with known anatomy.

Initial weak label extraction, A4C view. The final UNet trained for A2C prediction was used to predict segmentations for A4C images (resulting in predictions with two LAs and two LVs per image). Centroids were calculated for each segment and known anatomical relationships leveraged to re-label these chambers as RA, RV, LA, and LV. Shape and topological descriptors were used to discard images whose segmentations failed relationship, size, and eccentricity thresholds, and which lacked four connected components.

During pipeline training for A4C, intermediate predictions on the validation set were noted to have systematically shorter RV length than appropriate. Intermediate predictions were therefore refined based on clinical spatial priors as follows. Length of the predicted LV and RV segments were measured, and its ratio β (RV height/LV height) computed. If the ratio β was less than 0.8, that is RV height was 80% of the LV height value or smaller, the RV segment was stretched to be proportional to the LV.

Initial weak label extraction, SAX view. A median blur filter (kernel size = 9) was applied to images to reduce noise and a Laplacian operator (kernel size = 5) was employed to extract edges and to reduce the amount of data in the image, an important step to reduce the computation time

of the Hough transform. Finally, the Hough circle transform³ was applied to detect the center and the radius of the endocardial region. Parameters for the Hough transform were a minimum distance between the centers of the detected circles of 400, minimum and maximum circle radius of 20 and 80, respectively.

Neural network architectures. *Quality control for segmentations during network training.*

A2C: Cutoffs for area were 6 to 75cm² for LA and RA, and 4.7 to 104cm² for LV and RV.

Acceptable eccentricities were 0.3-0.96 for LA, 0.17-0.95 for RA, 0.62-0.96 for LV, and 0.65-0.96 for RV. Connected components analysis required two chambers for the A2C view (an LA and an LV), and four chambers for the A4C view (LA, RA, LV, RV).

Table S1: Correlation, bias, accuracy, and kappa values.

Test set	Measurements Comparison	N	Regression analysis		BA analysis		NI vs abnl	
			r	r ²	Bias	LOA	Accuracy	Kappa
LVEDV (mL)								
All-comers	Echo vs AI	5665	0.84	0.70	2.26 mL	±50.9 mL	0.87	0.57
CMR subset	Echo vs SSL	485	0.69	0.69	-2.34 mL	±63.1 mL	0.8	0.57
CMR subset	CMR vs SSL	485	0.78	0.60	-57.49 mL	±108.4 mL	0.83	0.6
CMR subset	CMR vs Echo	485	0.82	0.67	-59.58 mL	±96.4 mL	0.78	0.51
Clinical variability	literature	50	--	--	23.0 mL	±42mL	--	--
Supervised learning	literature	337	--	0.7	2.3 mL	±58mL	--	--
Supervised learning	literature	8457	--	0.65	2.0 mL	±56mL	--	--
LVESV (mL)								
All-comers	Echo vs SSL	5665	0.9	0.82	5.3 mL	±31.3 mL	0.81	0.54
CMR subset	Echo vs SSL	485	0.9	0.81	4.24 mL	±40.7 mL	0.81	0.62
CMR subset	CMR vs SSL	485	0.85	0.72	-29.5 mL	±93.8 mL	0.79	0.57
CMR subset	CMR vs Echo	485	0.87	0.76	-33.7 mL	±83 mL	0.78	0.57
Clinical variability	literature	50	--	--	11mL	±20mL	--	--
Supervised learning	literature	337	--	0.74	3.6mL	±41mL	--	--
Supervised learning	literature	8457	--	0.74	--	±39mL	--	--
LVEF (%)								
All-comers	Echo vs SSL	5665	0.81	0.65	-5.27 %	±14.6 %	0.97	0.79
CMR subset	Echo vs SSL	485	0.8	0.8	-4.01 %	±14.1 %	0.95	0.83
CMR subset	CMR vs SSL	485	0.79	0.62	-1.51 %	±21.8 %	0.91	0.68
CMR subset	CMR vs Echo	485	0.82	0.68	2.47 %	±20.4 %	0.91	0.68
Clinical variability	literature	50	--	--	8%	±18%	--	--
Supervised learning	literature	337	--	0.5	-1.9%	±21%	--	--
Supervised learning	literature	8457	--	0.46	-5%	±20%	--	--
LV mass (g)								
All-comers	Echo vs SSL	5138	0.75	0.56	13.4 g	±73.6 g	0.71	0.35
CMR subset	Echo vs SSL	49	0.82	0.67	8.7 g	±76.5 g	0.84	0.67
CMR subset	CMR vs SSL	49	0.57	0.32	19.96 g	±160 g	0.61	0.23
CMR subset	CMR vs Echo	49	0.51	0.26	11.1 g	±169 g	0.61	0.23
Clinical variability	literature	60	--	--	8.7g	±49g	--	--
Supervised learning	literature	337	--	--	--	±91g	--	--

LA volume (mL)								
All-comers	Echo vs SSL	2177	0.92	0.84	-0.14 mL	±20.1 mL	0.9	0.77
Clinical variability	literature	85	--	--	7mL	±13mL	--	--
Supervised learning	literature	4800	--	--	5mL	±3mL	--	--
RVEDA (cm²)								
All-comers	Echo vs SSL	381	0.83	0.69	-0.86 cm ²	±5.4 cm ²	0.91	0.54
RVESA (cm²)								
All-comers	Echo vs SSL	381	0.84	0.71	1.60 cm ²	±3.9 cm ²	0.72	0.26
RA volume (mL)								
All-comers	Echo vs SSL	1007	0.87	0.76	-2.10 mL	±21 mL	0.92	0.73

Echo = clinical echocardiogram measurements, SSL = self-supervised AI pipeline-derived measurements, LVEF = left ventricular ejection fraction, LVEDV = left ventricular end-diastolic volume, LVESV = left ventricle end-systolic volume, RVEDA = right ventricular end-diastolic area, RVESA = right ventricular end-systolic area, r = Spearman correlation coefficient, BA = Bland-Altman, LOA = 95% limits of agreement (two standard deviations), CMR = cardiac MRI. As in main Figure 3, clinical intra-observer references include Jacobs et al 2006 for LVEDV, LVESV, and LVEF¹⁴; Crowley et al 2016 for LV mass⁵²; and Mihaila et al 2017 for LA volume. Supervised learning references include Ghorbani et al 2020⁴¹ and Zhang et al 2018⁷.

Table S2. Model performance of LV segmentation in an external dataset.

Dataset	EchoNet dataset (Nb patients)	Average Dice Score, Diastole [95% CI*]	Average Dice Score, Systole [95% CI*]
EchoNet model †	EchoNet test set (1,277)	0.927 [0.925 - 0.928]	0.903 [0.901 - 0.906]
Our model	EchoNet test set (1,277)	0.886 [0.885 - 0.887]	0.851 [0.850 - 0.853]
	Whole dataset (10,030)	0.886 [0.885 - 0.887]	0.847 [0.845 - 0.848]

Nb = number

* Confidence intervals were computed using 10,000 bootstrapped samples

† Values for EchoNet test set were extracted directly from the paper⁸ since the EchoNet model is not available.

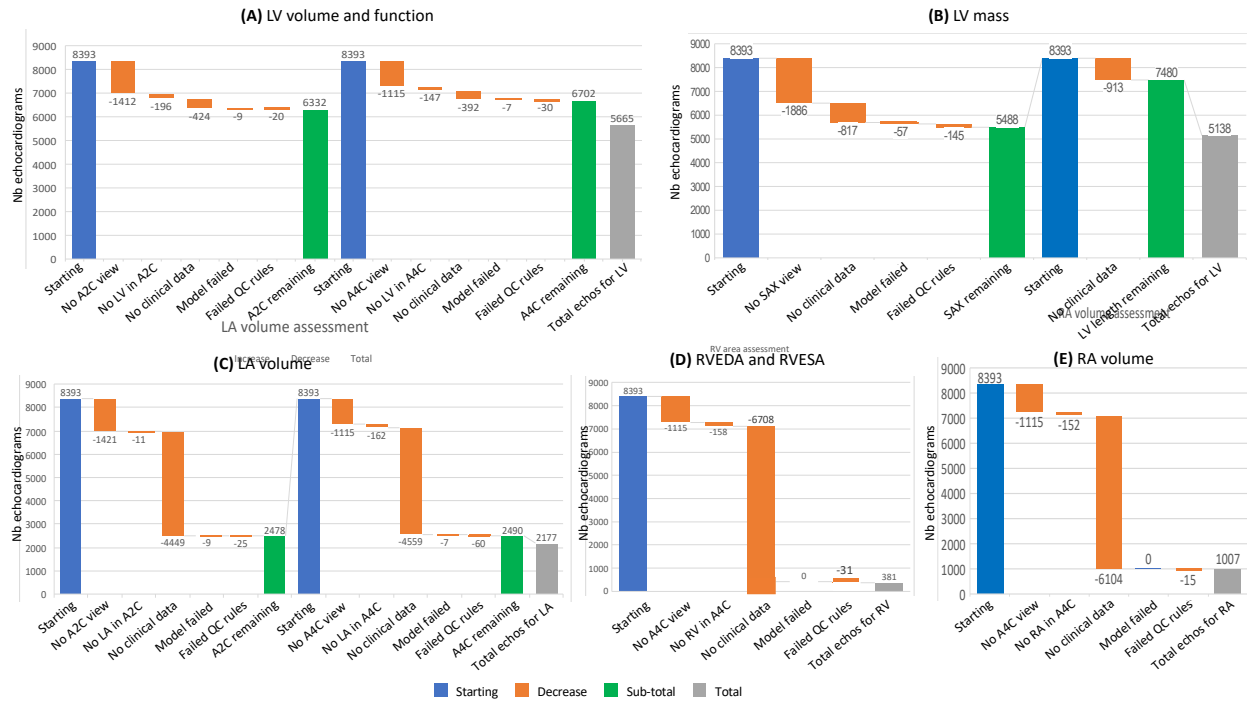


Figure S1. Inclusion/exclusion of test data by clinical measurement. The test set had 8,393 echocardiograms/patients. For each measurement assessed, certain views and chambers needed to be present in the echocardiogram as above; a clinical measurement needed to be present in the echocardiogram report for ground-truth comparison. (A) shows the echocardiograms containing A2C and A4C views and clinical ground-truth measurements of the LV for LV size and function assessments. (B) shows the echocardiograms containing SAX views of the LV and LV length measurement for LV mass assessment. (C) shows the echocardiograms containing A2C and A4C views/measurements of the LA, while (D) and (E) show the A4C views/measurements needed for RV and RA assessment, respectively. LV = left ventricle, LA = left atrium, RV = right ventricle, RA = right atrium, QC = quality control, A2C = apical 2-chamber view, A4C = apical 4-chamber view, SAX = short-axis mid view, Nb = number. “No clinical data” = no clinical echocardiogram measurement for comparison to ground truth, “Model failed” = model did not predict anything, “Failed QC rules” = model predicted a chamber, but its shape and/or size failed post-processing rules.

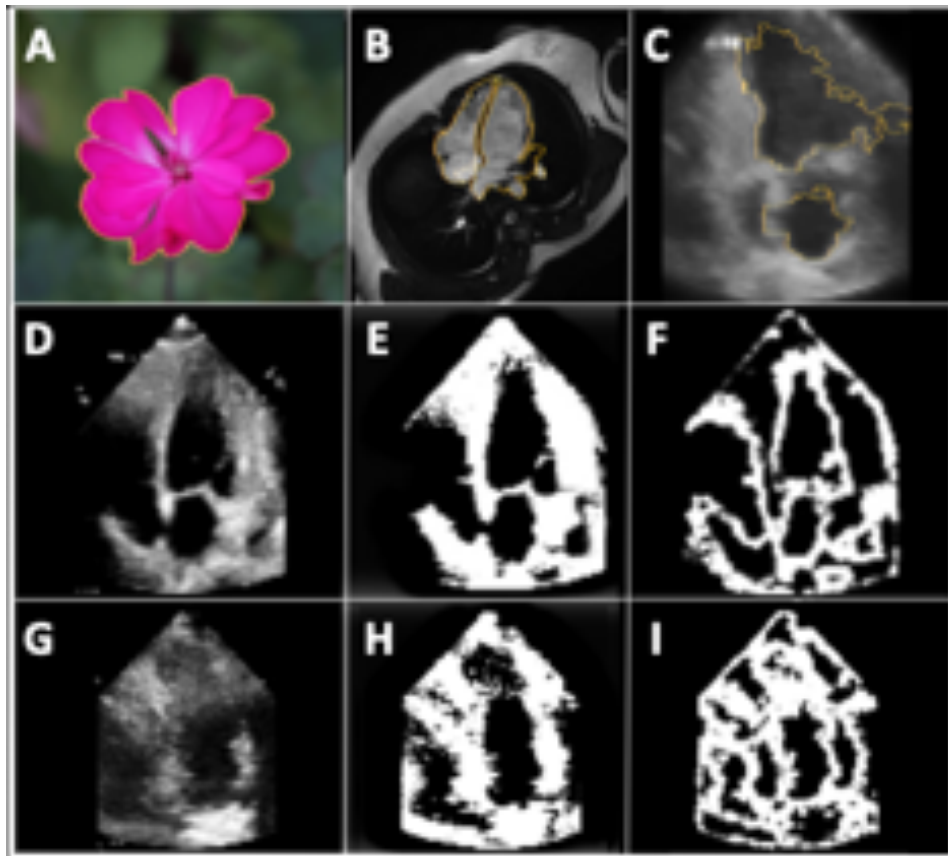


Figure S2. Examples of standard computer vision methods on different images. First row – classical computer vision watershed algorithm (thin yellow line) applied to (A) a photo image of a flower, and medical images of the heart in (B) MRI and (C) ultrasound modalities. Note that this algorithm works best on a photo image. Second and third rows depict two echo image examples – left (D,G): original echo images, middle (E,H): segmentation using bilateral filtering, right (F,I): segmentation using optical flow between consecutive frames of the echocardiography sequence.

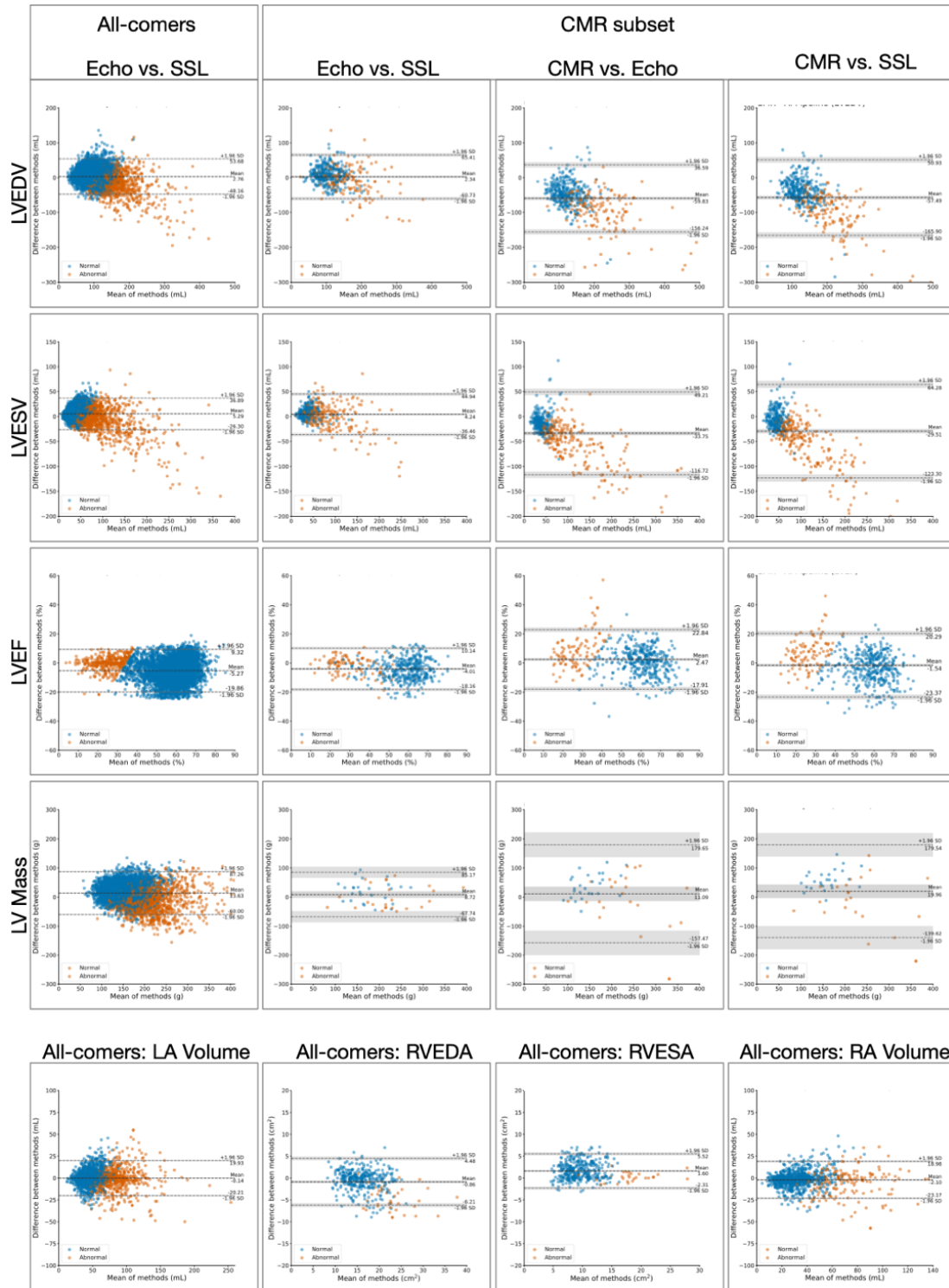


Fig S3: Bland-Altman plots. Blue dots represent normal measurements; orange dots, abnormal. SSL = self-supervised AI pipeline, CMR = cardiac MRI, LVEDV= LV diastolic volume, LVESV = LV systolic volume, LVEF = LV ejection fraction, RVEDA and RVESA = RV end-diastolic and -systolic areas, respectively.

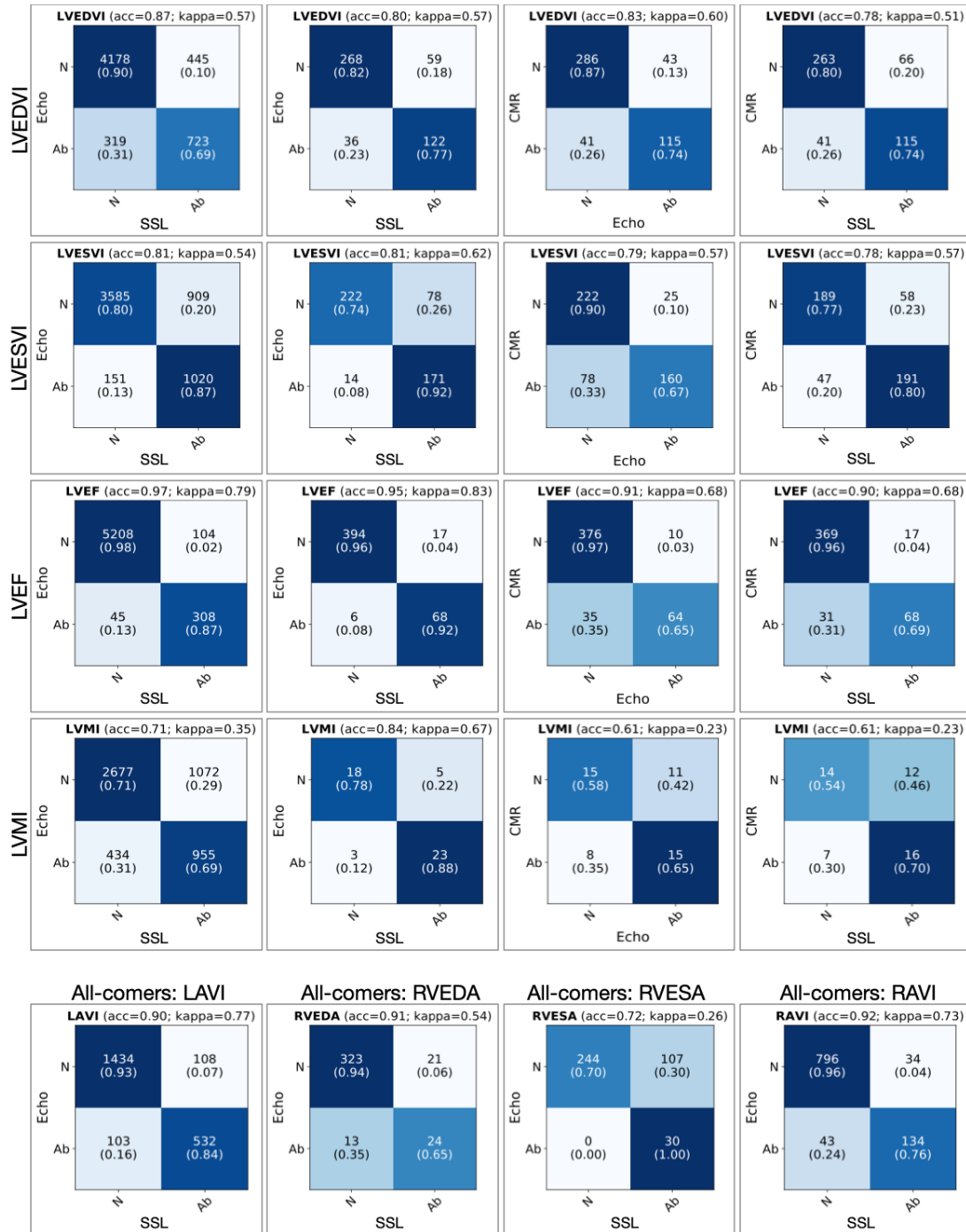


Fig S4: Confusion matrices for measurements binarized into normal (N) vs. abnormal (Ab).

Accuracy and Cohen's kappa are shown. Measurements are indexed by body surface area where clinically applicable. SSL = self-supervised AI pipeline, CMR = cardiac MRI, LVEDVI = LV diastolic volume index, LVESVI = LV systolic volume index, LVEF = LV ejection fraction, LVMI = LV mass index, RVEDA and RVESA = RV end-diastolic and -systolic areas, respectively, RAVI = RA volume index.

Supplemental References

1. Wu S, Zhu Q, Xie Y. Evaluation of various speckle reduction filters on medical ultrasound images. *Annu Int Conf IEEE Eng Med Biol Soc* 2013;2013:1148–1151. doi:10.1109/EMBC.2013.6609709.
2. Roerdink JBTM, Meijster A. The Watershed Transform: Definitions, Algorithms and Parallelization Strategies. *Fundamenta Informaticae* 2000;41:187–228.
3. Yuen H, Princen J, Illingworth J, Kittler J. Comparative study of Hough Transform methods for circle finding. *Image and Vision Computing* 1990;8:71–77. doi:10.1016/0262-8856(90)90059-E.